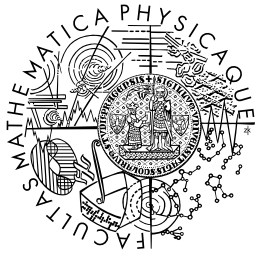

FACULTY
OF MATHEMATICS
AND PHYSICS
Charles University

BACHELOR THESIS

Martin Pavelka

Study of novel materials and nanostructures for spin photonics and electronics

Institute of Physics of Charles University

Supervisor of the bachelor thesis:	RNDr. Martin Veis, Ph.D.
Study programme:	Physics
Study branch:	General Physics

Prague 2017

I declare that I carried out this bachelor thesis independently, and only with the cited sources, literature and other professional sources.

I understand that my work relates to the rights and obligations under the Act No. 121/2000 Sb., the Copyright Act, as amended, in particular the fact that the Charles University has the right to conclude a license agreement on the use of this work as a school work pursuant to Section 60 subsection 1 of the Copyright Act.

In Prague 19.5.2017 signature of the author 

Title: Study of novel materials and nanostructures for spin photonics and electronics

Author: Martin Pavelka

Institute: Institute of Physics of Charles University

Supervisor: RNDr. Martin Veis, Ph.D., Institute of Physics of Charles University

Abstract: This work is dedicated to the study of two magnetic materials. Thin films of ferrimagnetic alloy Gd_xFe_{100-x} fabricated with different compositions near the compensation temperature $x \doteq 25$ by magnetron sputtering on Si substrate with the usage of Ru and SiO_2 capping layer were investigated. Measurements of the magneto-optic Kerr effect spectroscopy and magnetometry showed opposite signs in magnetization when the compensation temperature composition exceeded as well as the enhancement of the effect for SiO_2 capping layer. Spectroscopic ellipsometry revealed the complex diagonal element of the permittivity tensor. An attempt to prepare thin film of ferromagnetic tetragonal $D022 - Mn_3Ge$ was made. That was done firstly by calibrating Mn and Ge targets in magnetron sputtering machine and secondly simultaneous deposition of the elements on MgO (001) substrate with Cr buffer layer.

Keywords: magneto-optics, spectroscopic ellipsometry, sputtering, $GdFe$, Mn_3Ge

Firstly, I would like to express my gratitude to my parents and family for all the unlimited support, that I have been receiving not only during my studies, but ever since I was born.

Secondly, my gratefulness goes to all the people who helped me with this thesis and who contributed with their tools or measurements which made this work interesting and possible.
It is mainly Dr. Martin Veis who provided me with amazing scientific knowledge, options and experience.
My big thanks belongs also to Dr. Karel Vyborný for fruitful discussions about the Mn_3Ge material and to Dr. Andy Rushforth who hosted me in University of Nottingham with a great kindness.
My appreciation also goes to prof. Václav Holý and Mgr. Petr Cejpek who carried out the structural analysis of my samples.
And last but not least, I would like to thank Mgr. Lukáš Beran, Alex Lewis, MSc, Bc. Daniel Král and Mgr. Eva Jesenská for their friendship and help during the work in the laboratories and offices on this project.

Contents

Introduction

The aim of this thesis is to present a study of two novel magnetic materials which are promising for future applications in new technological concepts. These concepts are responding to the rapid development in computer science, where is a high demand for an increase of the speed of computer chips and data transfer as well as for an increase of data storage density. Current field of electronics based on the semiconductor transistor is starting to face its physical limits which it should fully reach before 2020. Spintronic devices, where the information is carried by the electron's spin instead of the charge, appear to be a promising replacement of the current generation of electronic devices. Moreover, a combination of spintronic concepts with photonic could allow the creation of a whole new platform of photonic devices for computer science of the future. Novel trends in the display technology require 3D holographic displays, which are designed for the use without the necessity of any additional glasses as used today. This thesis is dedicated to the study of novel materials and nanostructures suitable for these applications. Its outputs will help to bring novel spintronics and spin photonics concepts closer to the realization in proposed devices.

The main goals of the work is to use magneto-optic spectroscopy, magnetometry and spectroscopic ellipsometry for characterisation of the novel materials. The first task is the systematic study of properties of the thin films of gadolinium-iron alloy on silicon substrate prepared by the sputtering deposition method. This material has a potential to serve as the free layer in the spatial light modulator in the next generations of displays, which should provide 3D image with high definition resolution. The thesis describes the theory that lies behind the examination methods of thin layer samples, mainly from the optical and magneto-optic point of view. The second objective is to fabricate and examine Heusller compound Mn_3Ge using magnetron-sputtering and possibly obtain its optical and magneto-optic properties. This material has a high potential of application in a dense non-volatile magnetic memory storage as proposed by spintronics.

The first chapter introduces the theory, dealing with the introduction of basic optical phenomena as electromagnetic wave, its polarization and the vector and matrix representation of its properties. Basic magneto-optic effects are also introduced, as well as the basic theory of the interaction of light and solid-state materials.
The second chapter describes the used experimental methods in the form that had been used for measurements in the experimental section.
With the third chapter, the application concept, as well as the studied materials with the focus on the recent development are introduced. Each of the studied materials is very close to wide application in modern display technology and information technology, therefore we try to explain basic ideas of each materials implementation in the future devices.
The last chapter presents the results of the experiments conducted on studied materials $GdFe$ and Mn_3Ge, as well as an attempt of fabrication of the latter one.

1. Theory of light propagation and magneto-optic effects

In this chapter, we are going to introduce basic theoretical and mathematical tools for the description of light propagation and its interaction with matter, including special emphasis on magneto-optic effects.

1.1 Wave description of light

Wave description of light is based on the theory of classical electrodynamics, which phenomenologically describes electricity and magnetism. It was James C. Maxwell who had mathematically proven in 1864, that electric and magnetic fields propagate as electromagnetic wave and that the wave equation can be derived directly from his well-known Maxwell's equations. This set of four equations relate the speed of light with electric permeability and magnetic permittivity. Maxwell, based on the congruence of his theoretical prediction and the latest measurements of those constants, wrote: "The agreement of the results seems to show that light and magnetism are affections of the same substance, and that light is an electromagnetic disturbance propagated through the field according to electromagnetic laws [1]".

Maxwell's equations are fundamental for the wave description of light and every advanced optics textbook begins with their introduction [2]. Their general form (in the SI unit system), which is valid in all media is:

$$\nabla \cdot \mathbf{D} = \rho \,, \tag{1.1}$$

$$\nabla \cdot \mathbf{B} = 0 \,, \tag{1.2}$$

$$\nabla \times \mathbf{E} = -\frac{\partial \mathbf{B}}{\partial t} \,, \tag{1.3}$$

$$\nabla \times \mathbf{H} = \frac{\partial \mathbf{D}}{\partial t} + \mathbf{j} \,, \tag{1.4}$$

where $\mathbf{D}$ is a vector of the electric displacement field, $\mathbf{H}$ is a vector of the magnetic field intensity, ρ is the charge density and $\mathbf{j}$ is the current density. Equation 1.1 is the Gauss' law, which says, that an electric field arises from the electric charge as a conservative vector field (its divergence is non-zero). Equation 1.2 is the Gauss's Law for magnetism, stating the non-existence of magnetic monopoles and that the magnetic field is a solenoidal vector field (its divergence is zero at all points in the field). Equation 1.3 is well known as the Faraday's Law, describing how the change of the magnetic field in time induces electric field. Lastly Equation 1.4 is the Ampere's Law completed with revision by Maxwell, which again connects the electric and magnetic fields, including the electric current.

This set of the Maxwell's equation is usually completed with the constitutive relations which bind together the electric displacement field $\mathbf{D}$ with the electric

field $\mathbf{E}$, as well as the magnetic field intensity $\mathbf{H}$ and the magnetic field $\mathbf{B}$. There is also a relation between the electric field and the current density, generally known as the Ohm's law. In an isotropic material all these relations are denoted as:

$$\mathbf{D} = \varepsilon \mathbf{E}\,, \tag{1.5}$$

$$\mathbf{B} = \mu \mathbf{E}\,, \tag{1.6}$$

$$\mathbf{j} = \sigma \mathbf{E}\,, \tag{1.7}$$

where ε denotes the electric permittivity, μ the magnetic permeability and σ the electric conductivity. The most important prediction of the Maxwell's equations is the derivation of the wave equation [2]. By applying the curl operator onto Equation 1.3 or partial derivative with respect to time on Equation 1.4, by using vector identities and the relations 1.5, 1.6 and 1.7, we obtain the wave equation for the electric field $\mathbf{E}$. Its form in homogeneous, non-conducting media without any free charge is:

$$\Delta \mathbf{E} - \varepsilon\mu \frac{\partial^2 \mathbf{E}}{\partial t^2} = 0\,. \tag{1.8}$$

Analogous equation can be obtained for the magnetic field intensity $\mathbf{H}$. By comparing this equation to its general mathematical form, we get the already mentioned relation between the speed of light and electric and magnetic constants:

$$v = \frac{1}{\sqrt{\varepsilon\mu}}\,. \tag{1.9}$$

One of the solutions of the wave equation for the electric field is the monochromatic plane harmonic wave solution, which can be denoted in the complex symbolic as:

$$\mathbf{E}(\mathbf{r}) = \mathrm{Re}\left\{\mathbf{E_0} \exp[-i(\omega t - \mathbf{k}\cdot\mathbf{r} + \varphi)]\right\}\,, \tag{1.10}$$

where $\mathbf{r}$ is the position vector, $\mathbf{E_0}$ is the amplitude, ω is the circular frequency, $\mathbf{k}$ is the wave vector and φ is the initial phase of the wave. From hereby the electric field will be preferred over the magnetic field, because at optical frequencies the electric dipoles are responsible for the material response on the impacting light wave. Then the magnetic field can be calculated as the orthogonal supplement to the electric field and the wave propagation vectors.

1.2 Polarization of light

One of the basic properties of light is its polarization. It is the notion of what geometrical path the electric field vector follows as it oscillates. We assume that a monochromatic wave propagates in the direction of the axis z and the electric field vector can be decomposed into two scalar functions E_x and E_y in the unit directions of the axes $\mathbf{x}$ and $\mathbf{y}$ as:

$$\begin{aligned} \mathbf{E}(\mathbf{z},t) &= E_x\mathbf{x} + E_y\mathbf{y} \\ E_x &= a_x \cos\left[\omega\left(t-\frac{z}{v}\right)+\varphi_x\right] \\ E_y &= a_y \cos\left[\omega\left(t-\frac{z}{v}\right)+\varphi_y\right] \end{aligned} \tag{1.11}$$

By using the sine/cosine identities, subtracting the formulas for E_x and E_y and defining the phase $\varphi \equiv \varphi_y - \varphi_x$ we obtain the equation of ellipse [2] :

$$\left(\frac{E_x}{a_x}\right)^2 - 2\frac{E_x}{a_x}\frac{E_y}{a_y}\cos\varphi + \left(\frac{E_y}{a_y}\right)^2 = \sin^2\varphi\,, \tag{1.12}$$

which shows that the vector of electric field in a certain point $z = const.$ oscillates in an ellipse-shaped trajectory in the (x, y) plane.

Description of an ellipse

Equation 1.12 is in the form of the ellipse formula and therefore we can describe the geometry of the electric field oscillations with following geometrical quantities (compare with Figure 1.1):

- The *major axis* a and the *minor axis* b of ellipse define its shape. Ratio of these is so called the *ellipticity*, defined as $e = \frac{b}{a} = \tan\chi$, where the *ellipticity angle* $\chi \in (-\frac{\pi}{4}; \frac{\pi}{4})$ is also an equivalent notion how much is an ellipse elliptic.
- Rotation of the ellipse with respect to its major axis horizontal axis is described by the *azimuth* $\Psi \in (-\frac{\pi}{2}; \frac{\pi}{2})$ angle.
- The *amplitude* of the wave is defined as $E_0 = \sqrt{a_x^2 + a_y^2}$.

For the description of the state of polarization we only need information about the ellipticity and the azimuth.

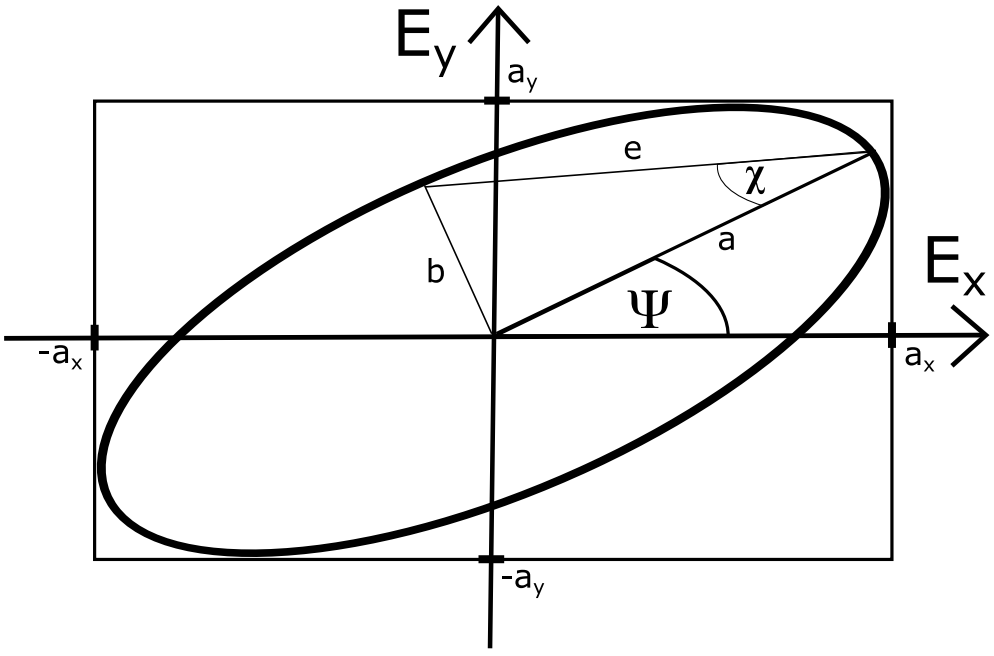

Figure 1.1: Diagram of polarization ellipse.

There are two main special cases of polarization:

- The light becomes linearly polarized when one of the axis intensities vanishes, that is when $a_x = 0$ or $a_y = 0$; or when the phase difference is $\varphi = 0$ or $\varphi = \pi$.
- The circular polarization is the case of polarization when the ellipse becomes a circle (that means $a_x = a_y = a_0$) and the phase difference is $\varphi = \pm\frac{\pi}{2}$. In our convention, for the positive sign we call this state the right circular polarization and for the negative sign the left circular polarization.

Jones formalism

One of the most practical way to describe and calculate the polarization state of light in a certain optical system is the calculus of Jones vectors and matrices in the complex plane representation. The alternatives to this formalism of polarization description include the Poincaré sphere, the Mueller matrices, the coherence matrix or the Stokes vectors, but for our case the Jones formalism is the most useful (it describes only fully polarized light, yet it gives a good insight about the experimental configuration and the explanation of studied effects).
Firstly, we define the complex amplitudes $A_{x,y}$ of the x and y components and the Jones vector $\mathbf{J}$ of a wave propagating in the direction of the axis $\mathbf{z}$ as:

$$A_{x,y} = a_{x,y} \exp(-i\varphi_{x,y}) \,, \tag{1.13}$$

$$\mathbf{J} = \begin{bmatrix} A_x \\ A_y \end{bmatrix} . \tag{1.14}$$

For practical use we always assume that Jones vectors are normalised (that is $|A_x|^2 + |A_y|^2 = 1$) and for most of the cases, we neglect the information about the phase in $t = 0$ and set it $\varphi_x = 0$. The special cases of the polarization are denoted in this formalism as follows:

- the linear polarization along the axis $\mathbf{x}$

$$\mathbf{J_x} = \begin{bmatrix} 1 \\ 0 \end{bmatrix} , \tag{1.15}$$

- the linear polarization under angle θ with respect to axis $\mathbf{x}$

$$\mathbf{J_x} = \begin{bmatrix} \cos\theta \\ \sin\theta \end{bmatrix} , \tag{1.16}$$

- the right/left circular polarization

$$\mathbf{J}_\pm = \frac{1}{\sqrt{2}} \begin{bmatrix} 1 \\ \pm i \end{bmatrix} . \tag{1.17}$$

These polarization states can be changed by n optical components in path of the ray, which are in the sequence of the propagation described by Jones matrices

$\mathbf{T}_1$,...,$\mathbf{T}_n$. This change of the original input polarization $\mathbf{J_I}$ into a new output polarization $\mathbf{J_O}$ is characterised by the matrix product:

$$\mathbf{J_O} = \mathbf{T}_n ... \mathbf{T}_1 \mathbf{J_I} \,. \tag{1.18}$$

These basic Jones vectors can also be used as a basis for further changes of the polarization state in order to make our calculations easier. As we are using mainly the linear polarization of light in later chapters, next list represents the Jones matrices of the most important optical components in the Cartesian representation. These matrices are introduced as follows in [3]:

- a linear polarizer rotated by angle α with respect to axis $\mathbf{x}$

$$\mathbf{P} = \begin{pmatrix} \cos^2\alpha & \sin\alpha\cos\alpha \\ \sin\alpha\cos\alpha & \sin^2\alpha \end{pmatrix} , \tag{1.19}$$

- a phase plate (linear retarder) with phase difference δ

$$\mathbf{R} = \begin{pmatrix} e^{i\frac{\delta}{2}} & 0 \\ 0 & e^{-i\frac{\delta}{2}} \end{pmatrix} , \tag{1.20}$$

- an element rotating the polarization by angle η

$$\mathbf{N} = \begin{pmatrix} \cos\eta & -\sin\eta \\ \sin\eta & \cos\eta \end{pmatrix} . \tag{1.21}$$

1.3 Anisotropic media and magneto-optic effects

The previous description of the propagation of light was related to the free space or media that are homogeneous and isotropic - all their properties are the same in all directions and do not change in any part of the investigated space. Yet the power of light as a material research tool lies in its interaction with media, which change light's properties (especially its polarization) as the rays propagate in the different directions. Such media are called anisotropic and can be well described by the permittivity tensor.

Permittivity tensor

In the first part of this chapter we introduced Equations 1.5 and 1.6 without any further details. The second equation does not offer much new information for studying of the optical phenomena, because the relative magnetic permeability is on the optical frequencies for most materials $\mu_r \sim 1$. Yet the electrical permittivity ε can be in the homogeneous isotropic materials treated as a scalar (as considered up until now), whereas in its general form it is a second-order tensor (a 3×3 matrix) with complex elements:

$$\overleftrightarrow{\varepsilon} = \begin{pmatrix} \varepsilon_{xx} & \varepsilon_{xy} & \varepsilon_{xz} \\ \varepsilon_{yx} & \varepsilon_{yy} & \varepsilon_{yz} \\ \varepsilon_{zx} & \varepsilon_{zy} & \varepsilon_{zz} \end{pmatrix} . \tag{1.22}$$

This tensor is proven to be symmetric [2], that means the off-diagonal elements are equal - in general, the optical properties of any material can be described by 6 complex numbers.

Magneto-optic effects

Magneto-optic (*MO*) effects are based on the disruption of the isotropy of the media caused by their magnetization **m**. For MO effects, as well as general optical effects, which involve the reflection and transmission of light, it is important to separate the material's response for s-polarization (which is linear polarization with the oscilation perpendicular to the plane of incidence) and the p-polarization (which is parallel to the plane of incidence). That is done in the Jones reflection matrix:

$$\mathbf{S} = \begin{pmatrix} r_{ss} & r_{sp} \\ r_{ps} & r_{pp} \end{pmatrix} , \tag{1.23}$$

where its elements are the amplitude reflection coefficients [4]. The diagonal elements are at the normal light incidence intertwined as $r_{ss} = -r_{pp}$ and even in magnetization. The off-diagonal elements are symmetric $r_{sp} = r_{ps}$, odd in magnetization. They also vanish in isotropic materials, but are non-zero in anisotropic media, because of the interaction between the s- and p-polarized waves.

Historically, it was Michael Faraday, who in 1845 discovered the first MO effect, nowadays known as the **Faraday effect** (*FE*), which causes light's linear polarization to rotate its plane when transmitted through a substance with magnetic field along the ray propagation. This was the first observed effect to prove connection of light and magnetism. The FE can be used as an experimental tool to study various materials and is also employed in the MO isolators (which prevents the reflected light from returning to its source) or in the Faraday cells. The MO effect, that is highly important for this work, is observed in reflection configuration. It is the **magneto-optic Kerr effect** (*MOKE*), which was first recognised by John Kerr in 1876 and soon reported in [5] and [6].
For incident p-polarized wave we define the complex Kerr effect angle Θ_K, the Kerr rotation θ_K and the Kerr ellipticity ϵ_K based on the reflectivity matrix as:

$$\frac{r_{sp}}{r_{pp}} =: \Theta_K \approx \theta_K - i \cdot \epsilon_K \, , \tag{1.24}$$

Kerr effect can be observed in three basic geometries (showed in Figure 3.2), which describe the direction of magnetization **m** with respect to incident rays. These geometries reflect how the reflection matrix simplifies. For longitudinal geometry, the matrix **S** has bound off-diagonal elements $r_{sp} = -r_{ps}$ at any angle of incidence, for transverse geometry, the off-diagonal elements are zero at any angle of incidence and for polar configuration, the matrix becomes at nearly normal incidence symmetric [3].

In the polar geometry configuration (when the magnetization vector points in the direction of the axis **z**) the permittivity tensor simplifies into:

$$\overleftrightarrow{\varepsilon}_{polar} = \begin{pmatrix} \varepsilon_1 & -i \cdot \varepsilon_2 & 0 \\ i \cdot \varepsilon_2 & \varepsilon_1 & 0 \\ 0 & 0 & \varepsilon_1 \end{pmatrix} , \tag{1.25}$$

where both of the independent permittivity elements are complex numbers with real and imaginary parts:

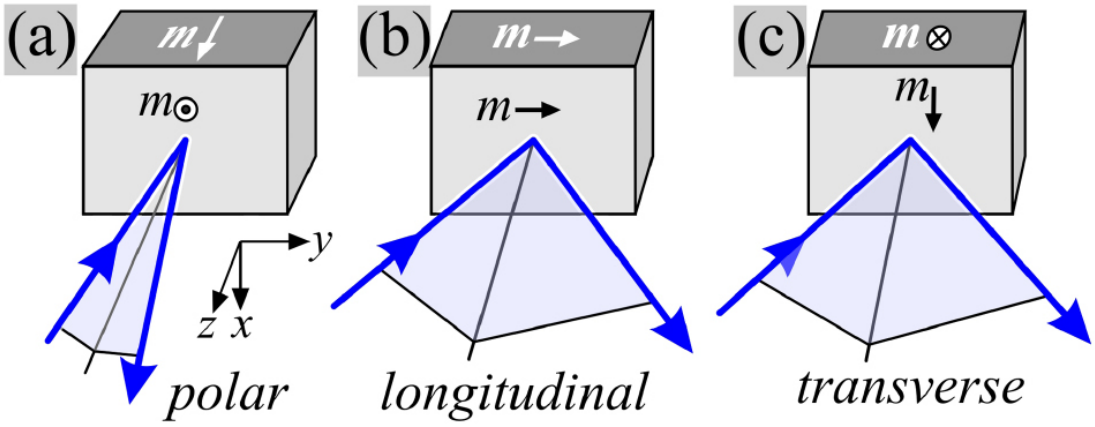

Figure 1.2: Possible geometries of Kerr effect [7].

$$\begin{aligned} \varepsilon_1 &= \varepsilon_{1r} - i \cdot \varepsilon_{1i} \,, \\ \varepsilon_2 &= \varepsilon_{2r} - i \cdot \varepsilon_{2i} \,. \end{aligned} \tag{1.26}$$

It is possible to derive the relation [3] between the polar Kerr effect and the permittivity tensor at the normal incidence:

$$\theta_K - i \cdot \epsilon_K \approx \frac{i\varepsilon_2}{\sqrt{\varepsilon_1}(\varepsilon_1 - 1)} \,. \tag{1.27}$$

For the advanced description of the interaction of light interaction with magnetic multilayered anisotropic media, the Yeh's formalism had been developed. This calculus introduces 4×4 matrices for description of layers' influence on the electric field of interacting light. It is derived from the substitution of the permittivity tensor into the wave equation. By using it, we can separate the information about the off-diagonal permittivity tensor elements of each layer from the observing experimental MOKE spectra. This formalism is used in advanced *MO* works, like [8].

The microscopical origin of the MOKE lies in the spin-orbit coupling and the exchange interaction in the magnetic materials in the magnetic field (similarly to the Zeeman effect). This fact is used in advanced research for ab-initio calculations.

The MOKE is for most of magnetic materials lower than one tenth of a degree, yet there are materials with the Kerr rotation of several degrees, like $PtMnSb$ [9], which is reported to have $\theta_K = 2.5°$. Besides of the most important use in the material research, the MOKE had been employed in the MO disks, where the writing of information is based on laser pulses heating the disk's plate above its Curie temperature and reading is mediated by analysing reflected linearly polarized pulses of lower intensity with respect to Kerr rotation.

2. Experimental methods

In this chapter we are going to introduce methods used for the sample characterization and deposition. Our main methods are based on MO and optical measurements in reflection, that provide us with information about the studied materials on the level of permittivity tensor, which is a direct manifestation of electron structure. These methods are supported by methods of the surface morphology examination and the structural analysis. We describe in detail also a method of fabrication of thin film samples, as the materials studied in experimental section of this work were prepared in the form of thin films.

2.1 Magneto-optic Kerr effect measurements

The MOKE, as described in the previous chapter, gives us an insight into the behaviour of media with a certain magnetization when exposed to an external magnetic field. Measurement of the MOKE has the advantages of good spatial resolution (but limited by wavelength of the incident light due to the diffraction limit), the depth resolution of 30 nm, a possible extension into vectorial measurements or time resolved measurements. Mainly, it is of non-destructive nature, as well as the cheap experimental assembly, without any special requirements on the sample preparation or vacuum [10]. This effect is widely studied especially in its spectral dependence, the magnetic field intensity dependence or observed with lateral resolution in magnetic domain Kerr microscopy. The first two cases are described in detail in the following subsection with a link to apparatus used in the experimental section of this work.

2.1.1 Magneto-optic Kerr effect spectroscopy

Using MOKE spectroscopy we study the spectral dependence of Kerr effect. That means we measure how the Kerr rotation and the Kerr ellipticity change with different energy of photons, that are interacting with the sample placed in an external magnetic field (energies of photons are expressed in eV, because these the spectra reflect the band structure of the studied materials). Our experiment is built in the polar configuration and is using the crossed-polarizers method. This method detects the intensity of light on the output of the spectroscope's assembly (which is shown in Figure 2.1), while rotating the analyser. The intensity than changes according to the Malus' law as square of sine of the difference between polarizer and analyzer angle.

With an optical system like this the Jones formalism comes useful. It is used to describe the change of polarization of the used light (typically white light from a halogen lamp). The input light is horizontally linearly polarized at first (ensured by full-spectra transmitting polarizer) and then interacts with matrices of the spectroscope's components. Those are: the reflection matrix $\mathbf{S}$ of the sample, a linear retarder $\mathbf{R}$ with shift of phase δ and a linear polarizer rotated by an angle

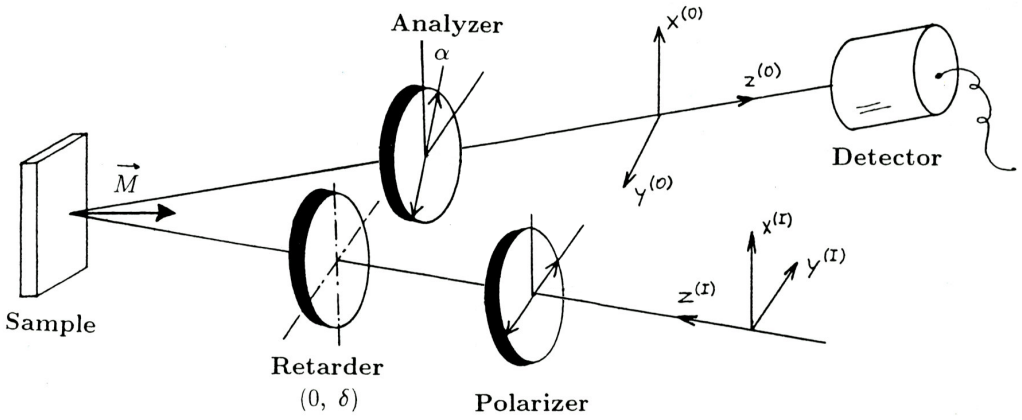

Figure 2.1: The crossed polarizers intensity method [3] (modified).

α with respect to the axis **x**. The light on the output from this system is:

$$\begin{aligned}\mathbf{J_1} &= \begin{pmatrix}\cos^2\alpha & \sin\alpha\cos\alpha\\ \sin\alpha\cos\alpha & \sin^2\alpha\end{pmatrix}\begin{pmatrix}\exp\left(i\frac{\delta}{2}\right) & 0\\ 0 & \exp\left(-i\frac{\delta}{2}\right)\end{pmatrix}\begin{pmatrix}r_{ss} & r_{sp}\\ r_{ps} & r_{pp}\end{pmatrix}\begin{pmatrix}0\\1\end{pmatrix}\\ &= \begin{pmatrix}r_{sp}\exp\left(i\frac{\delta}{2}\right)\cos^2\alpha + r_{pp}\exp\left(-i\frac{\delta}{2}\right)\sin\alpha\cos\alpha\\ r_{sp}\exp\left(i\frac{\delta}{2}\right)\sin\alpha\cos\alpha + r_{pp}\exp\left(-i\frac{\delta}{2}\right)\sin^2\alpha\end{pmatrix}.\end{aligned} \tag{2.1}$$

We detect intensity that is proportional to the norm of the Jones vector of the assembly's output as:

$$\begin{aligned}I \propto |\mathbf{J_1}|^2 =& |r_{sp}|^2\cos^2\alpha + |r_{pp}|^2\sin^2\alpha +\\ &+ r_{sp}r_{pp}^*\exp(i\delta)\sin\alpha\cos\alpha +\\ &+ r_{sp}^*r_{pp}\exp(-i\delta\sin\alpha\cos\alpha =\\ &= |r_{pp}|^2\left[|\Theta_K|^2\cos^2\alpha + \sin^2\alpha + \sin 2\alpha\,\mathrm{Re}\left\{\Theta_K\exp(i\delta)\right\}\right]\end{aligned} \tag{2.2}$$

which can be for small MOKE angles (based on the approximation $\Theta_K \approx \theta_K - i\epsilon_K$) simplified into:

$$I \propto |r_{pp}|^2\left[\sin^2\alpha + \sin 2\alpha\left(\theta_K\cos\delta + \epsilon_K\sin\delta\right)\right]. \tag{2.3}$$

Based on this equation, we are able to obtain merely the Kerr rotation (with the use of no linear retarder, since $\delta = 0$) or the Kerr ellipticity (with the use of a quarter-wave plate $\pi/2$).

With our laboratory's experimental setup, one is able to measure the MOKE down to resolution of 0.001°. Each measurement of MOKE spectra, typically ranging between energies of 1 to $5.5\,eV$ is executed in four regions: UV ($5.5 - 3.4\,eV$), VISA ($3.4 - 2.2\,eV$), VISB ($2.2 - 1.5\,eV$) and NIR ($1.5 - 1.1\,eV$). The assembly is also using four filters for those spectral segments in order to avoid the detection of higher order diffraction peaks in the monochromator. The intensity spectral detection is done by Shamrock SR-303i reflection grating monochromator

with CCD camera detector from 190 to 1100 nm by Andor. The detected signal is processed on a computer when for each rotation point of the analyser (typically set as 30 different angles) spectrum of intensity is fitted by the Cramer's rule as:

$$I(\alpha) = a_1 + a_2 \sin^2 \alpha + a_3 \sin 2\alpha \tag{2.4}$$

from which a plot of the Kerr rotation/ellipticity spectral dependence of θ_K and ϵ_K is done. The Kerr ellipticity is obtained by placing two quarter-wave plates in front of the detection unit.

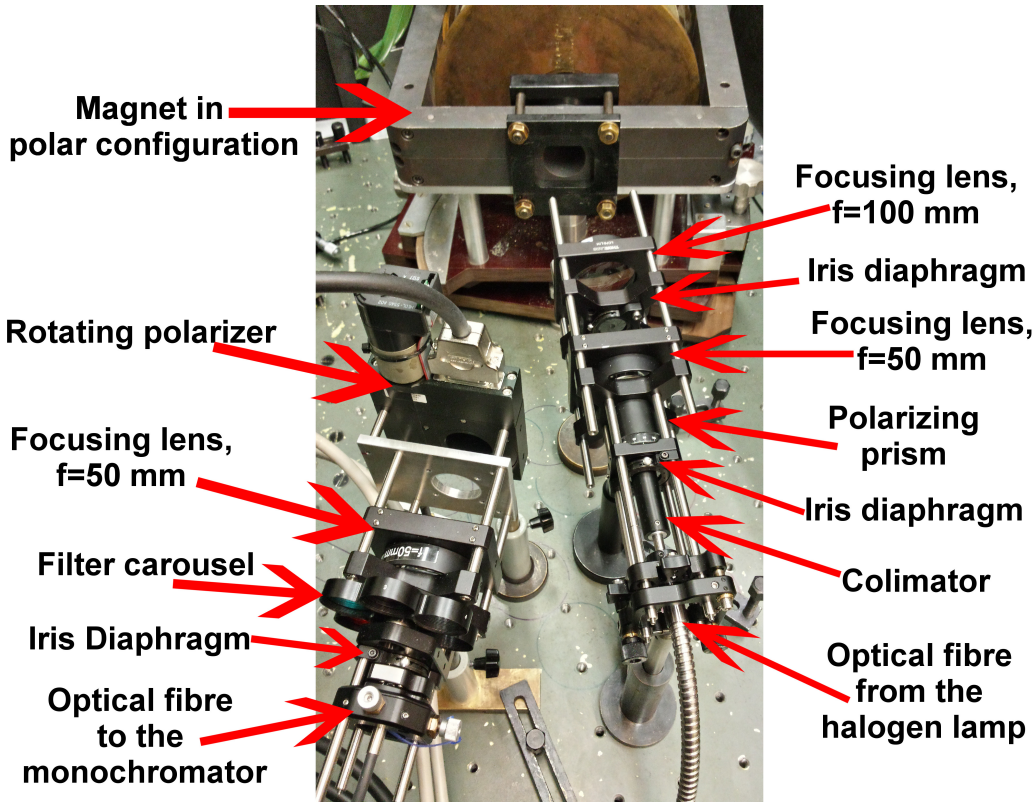

Figure 2.2: The assembly of the Kerr effect spectral dependence measurement.

An alternative for the crossed-polarizers method is the modulation method which can be used in MOKE spectra measurements for its high sensitivity, although this is counter-compensated by a more difficult built of the set-up with a need of frequent calibration. Our apparatus in the cross-polarizer configuration has proven to be faster, easier to use and provides us with an equal quality of the experimental data.

2.1.2 Magneto-optic Kerr effect magnetometry

MOKE magnetometry focuses on the Kerr effect using one wavelength rather than on spectral dependence of Kerr rotation. The MOKE's dependence on the intensity of the magnetic field $\mathbf{H}$ applied on the sample provides us with an equivalent information of a $\mathbf{m} - \mathbf{H}$ hysteresis curve of the studied magnetic material, which shows most importantly the saturation point $\mathbf{H}_S$ and the coercive field $\mathbf{H}_C$. That is the intensity of the magnetic filed, when the Kerr rotation

reaches its maximum and increases any further with increasing of the field intensity, respectively an ability of the studied material to stay magnetised without an external magnetic field. It is important to select a wavelength, that has the biggest Kerr rotation from the whole spectra in order to obtain the best signal. MOKE hysteresis curves can be typically obtained by the differential intensity detection in combination with the Wollaston prism (which separates s- and p-polarized light of the reflected light). This set-up is schematically shown in the figure 2.3. The normalised difference of the intensities I_1 and I_1 of the orthogonal polarizations is calculated and is proportional to the Kerr effect:

$$\Delta I = \frac{I_1 - I_2}{I_1 + I_2} \approx R[-(\theta_K + \alpha)\cos\delta + \epsilon_K \sin\delta]\,, \tag{2.5}$$

where R is a calibration constant. By using no linear retarder ($\delta = 0$) we obtain a direct information about the Kerr rotation.

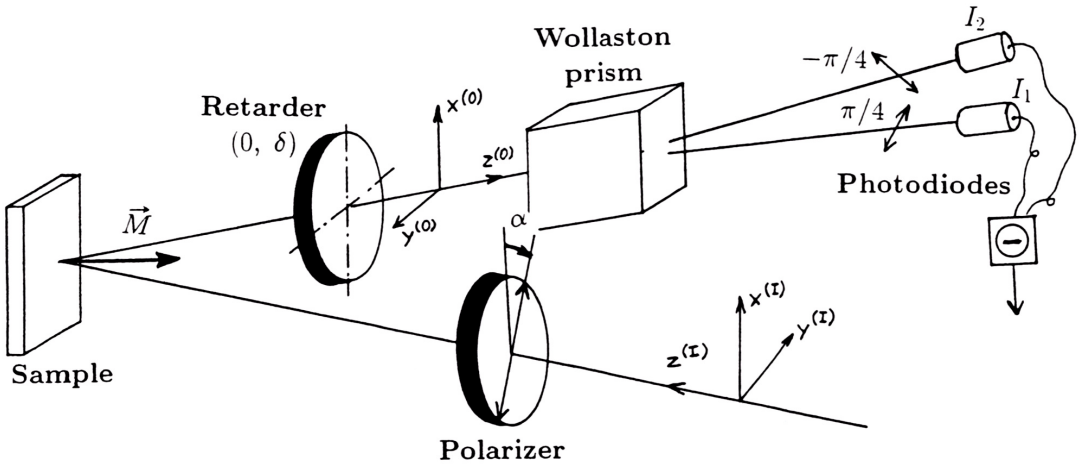

Figure 2.3: The differential intensity method with the Wollaston prism [3].

As the light source for *MOKE* magnetometry, our laboratory is using 3 different semiconductor laser diodes, which generate wavelengths (energies of photons) of $405\,nm$ $(3.06\,eV)$, $520\,nm$ $(2.38\,eV)$ and $658\,nm$ $(1.88\,eV)$ with $5 - 20\,mW$ output. These diodes are connected to a source of DC voltage and equipped with Peltier device for cooling and thermal stabilization. To secure clean linear polarization of the light, a polarizer is placed after the laser's aperture, as well as a lens to collimate the beam onto a sample placed into electromagnet in the polar configuration, which is powered by current up to $7\,A$, generating magnetic field up to $1.2\,T$. The magnetic field is measured with a Hall probe. As the detection unit, we are using two photodiodes placed behind an iris diaphragm (used to remove reflected depolarized stray rays), lens and mainly the Wollaston prism. The signal from both diodes is digitalised and ratio of their difference and their sum is plotted as the magnetization curve based on the equation 2.5. For samples with a small Kerr rotation a lock-in amplifier for the signal processing is required.

Overall, this method is a good alternative to the vibrating sample magnetometry or the superconducting quantum interference device, because it provides

quick, precise measurements of mainly ferrimagnetic materials, with option of real-time plotting of the magnetisation curve and microscopic lateral resolution. The mentioned methods are useful for materials with a weak magnetization. The main requirement for the sample is on its sufficient reflectivity.

2.2 Spectroscopic Ellipsometry

Spectroscopic ellipsometry (*SE*) is a powerful method to study both optically isotropic and anisotropic thin layer samples, especially those consisting of multiple layers. The basic observable of ellipsometry is the complex ellipsometric ratio ρ, which constitutes of the ellipsometric angles ψ (that expresses the ratio of the amplitudes of reflected s- and p-polarization) and Δ (that expresses the phase difference of the reflected s- and p-polarization), which are related to the diagonal elements of the reflection matrix as follows:

$$\rho = \tan\psi \cdot \exp(i\Delta) = \frac{r_{pp}}{r_{ss}}\,. \tag{2.6}$$

One is able, based on the ellipsometric angles measurements of a sample with known chemical composition, to quickly determine the thickness of sample's multiple layers and the interface roughness. The measurement is then related to the diagonal element ε_1 of the permittivity tensor (as introduced in the previous chapter), which is a complex number, whose real and complex parts are denoted as:

$$\varepsilon_1 = \varepsilon_{1r} + i\varepsilon_{1i}\,. \tag{2.7}$$

This quantity, which determines index of refraction in ε_{1r} and absorption in ε_{1i} can be obtained by fitting of experimental data of the ellipsometric angles ψ and Δ with theoretical models. These theoretical models are based on the theory of the Lorentz and Drude model.
There are more various optical systems which provide us with ellipsometric angles measurements, one typical is the **polarizer–compensator–sample–analyzer** (*PCSA)* in reflection mode as shown in Figure 2.4. This method detects intensity of light reflected from the sample after passing through the analyzer. Similarly to MOKE spectra, this method uses the crossed-polarisers method to determine ρ from the detected intensity. Our laboratory uses the Muller matrix ellipsometer Woollam RC2 with dual rotating compensators and multichannel detection working in photon energy range from 1.24 to 6.5 eV.

2.3 Atomic Force Microscopy

Atomic force microscopy (*AFM)* is a 3-dimensional surface imaging technique based on measuring of repulsive forces between the surface of a sample and the tip of an enclosed microcantilever. This cantilever is placed on a fine spring and is scanning the surface of the sample, while its height is monitored with reflected beam of a laser as depicted in Figure 2.5. By scanning the surface we can directly observe the morphology of the sample's surface atomic structure. For our measurements, we used this method to obtain the information about

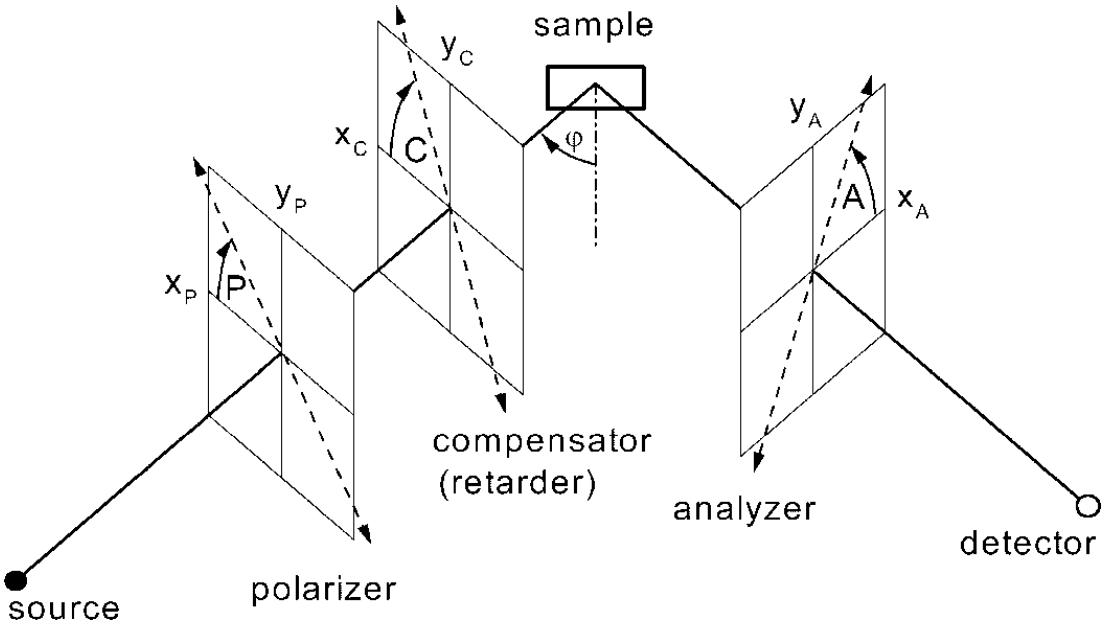

Figure 2.4: Polarizer–compensator–sample–analyzer (PCSA) configuration of an ellipsometer [11].

the surface roughness of the surface of certain samples. That is an important information for the fitting of the ellipsometric models, as well as a check of the sample fabrication's quality. AFM is one of scanning probe microscopy methods, similarly to scanning tunnelling microscopy or magnetic force microscopy. The latter one is an important technique for the research of the magnetic materials, because it is an alternative to the Kerr microscopy domain imaging, especially for the material with dense domains with the size smaller than the optical limit.

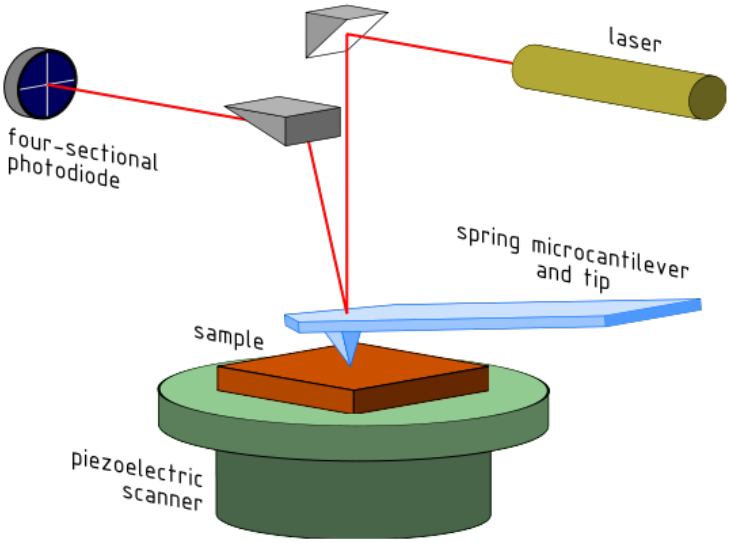

Figure 2.5: Schematic of an atomic force microscope with optical detection of the deflection of the microcantilever [12].

2.4 X-Ray Diffraction

X-ray diffraction (XRD) is the main method of the structural analysis. It provides us with information about the atomic ordering of the examined solid matter. We are most importantly able to obtain the lattice constant d of the poly- or single- crystalline phase of the studied sample from the observation of n diffraction maxima at angles θ, based on the Bragg's law:

$$n\lambda = 2d\sin\theta\,, \tag{2.8}$$

where λ is the wavelength of the X-ray, typically used spectral line of copper cathode Cu_{K_α} with $\lambda = 0.154\,nm$. A special type of the XRD measurement is the **X-ray reflectivity** (XRR), which is surface-sensitive X-ray scattering technique, important for the studying of the multiple layer thickness. It is based on the law of Fresnel reflectivity. We observe the oscillations of detected intensity while varying small angles of incidence of the X-ray . This measurement gives us information about the thickness of each layer (down to $0.1\,nm$ resolution), the roughness of the interlayer and the material density of the layer. This details are obtained by fitting the reflectivity intensity dependence based on the knowledge of the approximate electron density of each of the layers.

2.5 Sputtering

The sputtering thin film deposition technique is one of the most commonly methods used for thin films fabrication, when material's atoms are deposited on a substrate. The definition of a thin film is: "Low-dimensional material created by condensing, one-by-one, atomic/molecular/ionic species of matter [13]". The sputtering process (see Figure 2.6) uses the irradiation of energetic species from a gas discharge, when the removed particles (sputtered species) gain energies ranging between $1-10\,eV$. A **direct current** (DC) diode, a **radio frequency** (RF) diode, a magnetron diode, and ion beam are typically used for the ignition of the discharge. That happens in the sputtering chamber filled with the Ar gas, whose energetic ions then bombard the solid surface of a target. The target is typically composed from a pure element or an alloy, that are meant to be deposited on the substrate.

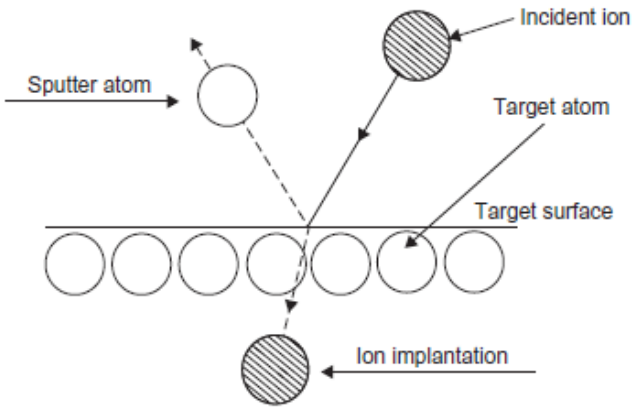

Figure 2.6: The physical sputtering processes [13].

Figure 2.7 shows the geometric configuration of two commonly used constructions of the sputtering machines. The DC diode system uses two planar electrodes. A cold cathode is placed under the target and is equipped with water cooling. An anode is placed above the substrate. This method is intended for metal targets, whereas insulators need an RF source. In order to lower the sputtering pressure and increase the sputtering rates, the magnetron sputtering source is required, because it is able to increase the plasma density of the discharge by its magnetic field. The magnetron can be built in cylindrical or planar geometry, with the later typically used. The magnetron is also used in combination with DC and RF diodes in magnetron sputtering machines. Typical sputtering machine has multiple targets with sources placed in confocal geometry for the option of co-sputtering.

Sputtering machines require a main chamber with ultra-high vacuum (UHV), with base pressure around $10^{-7}\,mTorr$, which is substituted with work pressure of an inert Ar or Kr gas ranging from 0.1 to $10\,mTorr$. Combination of multiple targets with various sources are usually used for the option to grow multiple layers of various compositions or alloy samples with different chemical and stoichiometric composition.

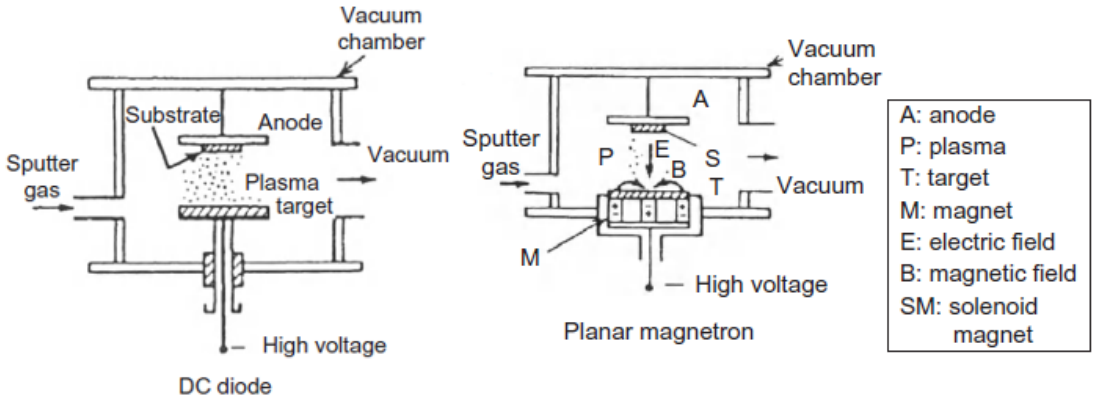

Figure 2.7: The basic configurations of the sputtering systems [13].

Methods alternative for the sputtering are pulsed laser deposition which is better for a more precise deposition of mainly thin layers of oxides or molecular beam epitaxy which is the most precise thin film growth method, allowing fabrication of samples with the precision of a single atomic layer.

3. Investigated materials and principles of their application

This chapter introduces the concepts behind certain areas of the current material research and also those materials, that were studied in the experimental chapter of this work.

3.1 Spin electronics and photonics

It was Otto Stern and Walter Gerlach, who in 1921 experimentally discovered, that electron has a property of quantization in two different orientations. This property - the spin, was theoretically explained by the Dirac's equation of relativistic quantum mechanics. Spin electronics (shortly called *spintronics*) aims to use this property in order to improve vantages of already existing electronic devices. In this subsection, we draw a brief insight into the reasons and background behind this recently emerging area of research and engineering.
The current situation in the field of information technology is suggesting a need for multiple substantial conceptual changes. There is a high demand on the improvement in the data transmission, processing and storage. Technology seeks its future realms in the utilization of up until recently in electronics ignored property of the electron - the spin. The basic ideas and goals of spintornics were formed around the year 2000 [14]. The spintronic concepts find also application in the newly founded field of the spin photonics. The main motivation for measurements in this thesis is the investigation of materials with perspective applications based on the spintronic concepts.

3.1.1 Motivation, end of the Moore's law

The field of electronics has experienced a quick development since the discovery of transistor by John Bardeen, Walter Brattain, and William Shockley in 1947 and its use in the integrated circuits as the thin film transistor. Today, the global electronics industry is worth approximately 1 trillion U.S. dollars. This technological and economical progress is closely connected to the Moore's law, which is more of a self-fulfilling prophecy, rather than a law in its definition meaning. It states, that the number of transistors per square inch on integrated circuits doubles approximately every 18 months [15].
This so-called law, which has been a drive for the electronic industry's for over than five decades is facing quantum limits of conventional electronics principles and the trend in fabrication of semiconductor devices will be completely abandoned before 2020 [16] and has already been broken in 2016 [17]. That implies, that new physical principles in storing and processing information are needed in order to sustain the further technological and economical growth. The field of spintronics offers many possibly applicable effects and materials, that could be implemented into already existing devices.

3.1.2 Key concepts

Many propositions of spintronics include possible applications in devices with low operation energy, room temperature operation and zero power leakage. These characteristics are based on the collective behaviour of spin-polarized electrons. The key part of material science for spintronics is to find proper materials with needed physical properties for the implantation of the physical phenomena with respect to reachable epitaxial quality of the material. Current aims of spintronics are to create concepts, materials and devices for the future magnetic memories, spin transistors, possible quantum computer and various biomedical sensors. Fundamental physical phenomena based on the spin lie behind these possibilities.

Giant magnetoresistance (GMR) was the first effect explained and studied spintronics, it needed the consideration of the presence of spin effects in order to be fully explained. The GMR can be observed in thin structures with ferromagnetic layers separated by non-magnetic layer. The resistance of this structure depends on magnetic moments arrangement in the ferromagnetic layers - it is the lowest, when they are aligned and highest, when they are anti-aligned [14]. This effect finds its use in the spin valve reading heads of today's hard disk drives. Albert Fert and Peter Grünberg were awarded Nobel Prize in 2007 for their discovery of GMR.

Magnetic tunnel junction (MTJ) is a structure, where in between two ferromagnetic layer plates (free and reference layer) a dielectric layer (typically of MgO or AlO) is introduced. Electrons are tunnelling across this ferromagnet/insulator/ferromagnet junction. Measurement of the resistivity of this structure depends on the relative magnetization of both magnetic layers. This can be used for reading of the state at the free layer plate. Writing is provided by changing magnetization by the Spin Hall effect of the free layer. This has been applied in the **magnetoresistive random access memories** (**MRAM**), which are about to become a universal nonvolatile storage components, yet there is still a need for proper magnetic materials in order to ensure the favourable properties of the component. This effect is used as the **spin transfer torgue MRAM** ($STT\text{-}MRAM$), which is already commercially available [18].

Previously, most of the spintonic concepts were built using ferri- or ferromagnetic materials, but a new sub-field of antiferromagnetic spintronics was introduced [19], opening new possibilities for this not much applied type of materials. There has been recently done a significant experimental progress, especially with the implementation of storing information in the antiferromagnetic alloy semimetal $CuMnAs$ [20]. Memory components like that do not have any stray fields and cannot be disturbed by an external magnetic field, since they are antiferromagnetic.

3.1.3 Holographic display concept

The new field of the spin photonics combines plasmonic and spintronic approaches to dynamically change, control and enhance the MO response of certain photonics

elements.
One of the first proposed devices stemming from this concepts combination is the holographic display based on **magneto-optic spatial light modulator** *(MO-SLM)* [21]. This device could provide realistic 3D image reconstruction based on the holographic fringe-pattern with a wide viewing zone, $0.5\mu m$ pixel size and $15ns$ response implemented into the high-definition television [22].
The MO-SLM in a pixel of such a display is proposed to be the free thin layer of a magnetically active material, that reflects incident polarized light with the Kerr rotation of θ_K when magnetized in the direction out of the layer and with $-\theta_K$ when magnetized in the opposite direction [23]. The switching of the magnetization can be easily done in big scales, yet not so easily on the micron level. There has been proposed a novel device, which is driven by **spin transfer switching** (*STS*). The combination with the free magnetic layer in the STS MO-SLM provides switching in single pixels (shown in Figure 3.1). Such device operates utilizing spintronic effect of GMR with current perpendicular to plane of the layers. The pixel consists of multilayered structure. The free layer needs a small magnetic field in order to change its magnetization. Then there is the copper spacer layer and the pinned layer that needs on the contrary a large magnetic field for the magnetization switching. There is a copper electrode on the bottom and a transparent electrode on the top of this structure. The direction of the current applied on those electrodes then determines if the free layer reflects light with its polarization rotated with θ_K or $-\theta_K$. The whole pixel structure can be prepared on silicon substrate, insulated by dielectric SiO_2 and implemented into the display's matrix. For the successful implementation of MO-SLM into a pixel, high quality magnetic thin films of materials with strong MO response, low optical absorption and suitable, low energy consumption magnetization switching are required. One of already investigated materials for the free layer was Co_2FeSi, but it did not have sufficient Kerr rotation in the whole visible spectral range. The recent development had shown a functional 10×5 array of pixels prototype [24] using $GdFe$.

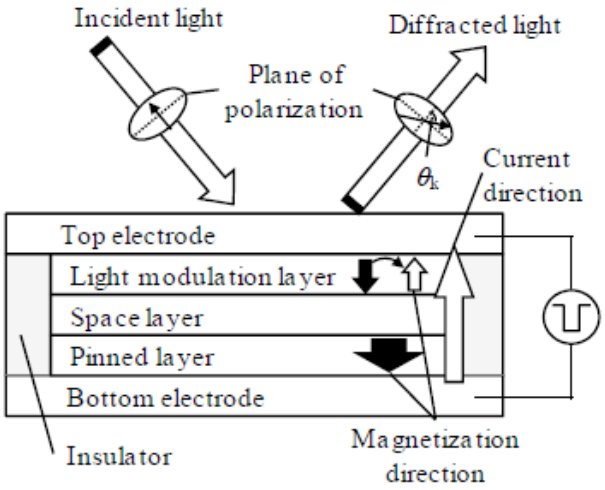

Figure 3.1: Illustration of the STS SLM and the MOKE [23].

3.2 $GdFe$ and background of its research

$GdFe$ is a ferrimagnetic alloy of rare earth and transition metal with different applications which are based on its typical magnetic structure (shown in Figure 3.2). This already well-studied material might find a new application in the *MO-SLM* based on its possible *STS* as a free layer [22], as it shows a reasonably large *MOKE*. That is also for its large magnetization density and the possibility to adjust its compensation temperature, coercive field and saturation magnetization by changing the composition [25]. Another valuable feature of $GdFe$ is that it enables the direct access to its spins through the electromagnetic interactions [26].

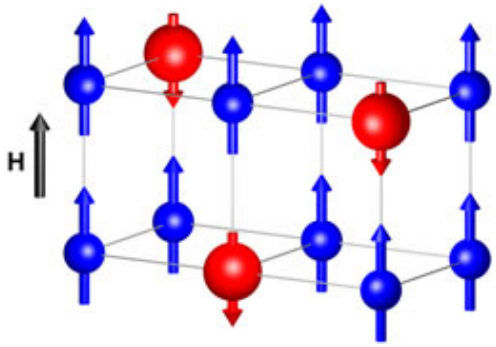

Figure 3.2: The magnetic structure of $GdFe$ (red= Gd, blue=Fe atoms) [26].

The compensation temperature of Gd_xFe_{100-x} is approximated to be $x \doteq 25$. This alloy of composition $Gd_{22}Fe_{78}$ was previously studied [25] prepared on a Si/SiO_2 substrate with Ru and SiN_x capping layers. This is to prevent the oxidation of the main layer. The latter capping enhanced the *MOKE* values through the whole spectra because of multiple reflections in the capping layer. The lattice mismatch of the two layers can also play a role, since it creates various strains. Further characterization of $GdFe$ with various compositions around the compensation point and different capping is needed in order to secure the best option for the application in the *STS MO-SLM* multilayer pixel.

3.3 Mn_3Ge and background of its research

Mn_3Ge is a perspective material for spintronics applications with at least three different phases possible at the room temperature. From the point of view of spintronic application Heusler alloy $D022 - Mn_3Ge$ (with its tetragonal structure shown in Figure 3.3) is of a deeper interest. That is because it can be a possible candidate for an application in the nanoscale MTJ in STT-MRAM due to its high perpendicular magnetic anisotropy. Recent work [27] presents details about the application in MTJ and the review [28] summarises different fabrication approaches.
The growth of the $D022 - Mn_3Ge$ on MgO substrate is described in series of papers from Sugihara's group [29, 30, 31, 32, 33, 34]. They showed the growth of this phase under different conditions, with different stoichiometry and buffer layers. There has been also a report of the growth of the $D022 - Mn_3Ge$ (001) prepared on the $SrTiO_3$ substrate [35]. It exhibited a low magnetization with high anisotropy, that can be tuned by a change in the stoichiometry.

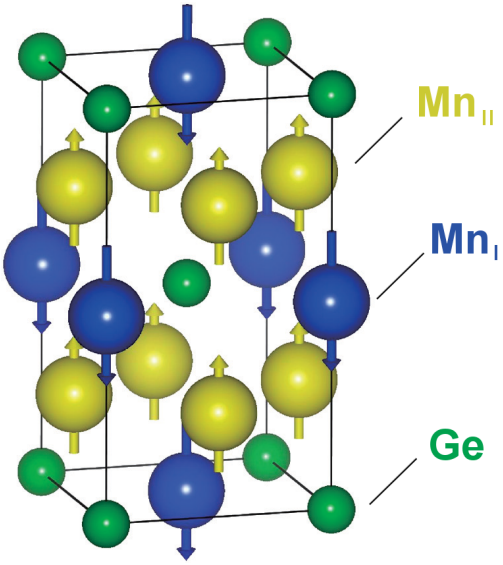

Figure 3.3: The crystal structure of the tetragonal $D022 - Mn_3Ge$ [29].

An another phase, the $D019 - Mn_3Ge$ has a hexagonal lattice structure with the non-collinear antiferromagnetic spin configuration and is also a subject of the recent research [36] for its strong anomalous Hall effect. Fabrication of the $D019 - Mn_3Ge$ should be achieved by deposition or crystal growth with temperatures over $750°C$ [37]. Another phase, the $\alpha - Mn_3Ge$ [38] exhibits ferrimagnetism and also seems to have possible application in spintronics. It is reported to grow at $150°C$ on $GaAs(001)$ substrates.

4. Studied samples and experimental results

4.1 $GdFe$

The aim of the study of provided $GdFe$ thin-film samples was to obtain MOKE spectra, MOKE magnetometry curves and SE data in order to derive information about the permittivity tensor of the studied layer.

4.1.1 Set of $GdFe$ samples

The sample fabrication was done by the research group in Japan who had previously in cooperation with our lab published paper [25] on previous set of samples. The results' outlines described are in the previous chapter. Measurement and study of this set of samples is focused on the further understanding of the influence of Gd to Fe ratio and also of the usage of two different capping materials. Investigated Gd_xFe_{100-x} thin layer samples were prepared by magnetron sputtering in Kr work gas atmosphere on Si substrate with surface layer of thermally oxidised SiO_2 using beam voltage 850 V with current 100 mA at the $Gd-Fe$ target and beam voltage 200 V with current 0-70 mA at the Gd target influencing the sample's composition x. The nominal thickness of $GdFe$ layer from the sputtering was $100\,nm$, however XRR measurement showed a slight variation from this value in all samples. To avoid the oxidation process, capping layer from Ru and SiO_2 were used for different samples. In Table 4.1 the overview of measured samples is listed.

Table 4.1: $GdFe$ samples with measured main layer thickness and with nominal thickness of capping layer

Sample designation	Substrate	Main layer	Capping
$x = 18.3\,Ru$	Si/SiO_2	Gd_xFe_{100-x} , $x = 18.3\,[136.9\,nm]$	Ru $[3\,nm]$
$x = 18.3\,SiO_2$	Si/SiO_2	Gd_xFe_{100-x} , $x = 18.3\,[136.9\,nm]$	SiO_2 $[20\,nm]$
$x = 20.0\,Ru$	Si/SiO_2	Gd_xFe_{100-x} , $x = 20.0\,[99.6\,nm]$	Ru $[3\,nm]$
$x = 24.7\,Ru$	Si/SiO_2	Gd_xFe_{100-x} , $x = 24.7\,[87.7\,nm]$	Ru $[3\,nm]$
$x = 24.7\,SiO_2$	$Si/SiO2$	Gd_xFe_{100-x} , $x = 24.7\,[87.7\,nm]$	SiO_2 $[20\,nm]$
$x = 26.7\,Ru$	Si/SiO_2	Gd_xFe_{100-x} , $x = 26.7\,[93.4\,nm]$	Ru $[3\,nm]$

4.1.2 Magneto-optic Kerr effect measurements

With MOKE spectra we have aimed to determine material's MO behaviour along the spectra ranging from 1 to $5.5\,eV$. We have conducted measurements of the Kerr rotation and ellipticity, with results shown in Figures 4.1a and 4.1b. These spectra show the approximately uniform Kerr rotation, which can be useful in future pixel implementation, when red, green and blue colours of incident light should be used to create chromatic spatial image. The spectra also clearly show

the enhancement of the effect in both rotation and ellipticity by the SiO_2 capping. Switch of the sign of the effect is also apparent for samples with Ru capping and composition with compensation temperature bellow room temperature. This is caused by the reorientation of the magnetic moments on each sub-lattice at the compensation temperature. This behaviour is typical for ferrimagnetic compounds.

We also measured hysteresis curves of all samples using three different wavelengths of the source light. These curves again show how composition influences magnetization of the layer. The easy axis of Gd_xFe_{100-x} magnetization lies out-of-plane for all the samples. The curves of not squared shape of hysteresis loops are farther from the compensation point and Gd_xFe_{100-x} magnetic sub-lattices saturates at different magnetic fields. The compositions near the compensation point exhibit higher coercitivity (the square shaped curves).
The purpose of this multiple hysteresis curves measurements was to observe if the shapes of the curves change with different photon energies. Such effect was observed in $Bi_3Fe_5O_{12}$ garnet thin film Faraday effect measurements of hysteresis curves [39]. In this work, authors present the explanation of the surprising hysteresis curve shapes as a superposition of two hysteresis curves with opposite sign. These curves should arise from each sub-lattice of the garnet. We predicted a possibility of analogous situation in $GdFe$, where magnetic moments of Gd and Fe are of different size. This effect for our $GdFe$ samples did not occur.
The measurements showed that only the amplitude of Kerr rotation changes with different photon energy (agrees with the MOKE spectra). The saturation intensities of magnetic field do not change with different photon energy. All the data correspond to the hysteresis MOKE spectra measurements. Important information about sample behaviour is the sign of the Kerr effect depending on Gd concentration and capping layer. By comparing Figures 4.4a and 4.4b, we see that samples with SiO_2 capping have more enhanced Kerr rotation than those with Ru top layer. That is caused, with the highest probability, by multiple reflections on interface SiO_2, which is also thicker compared to Ru coating layer.

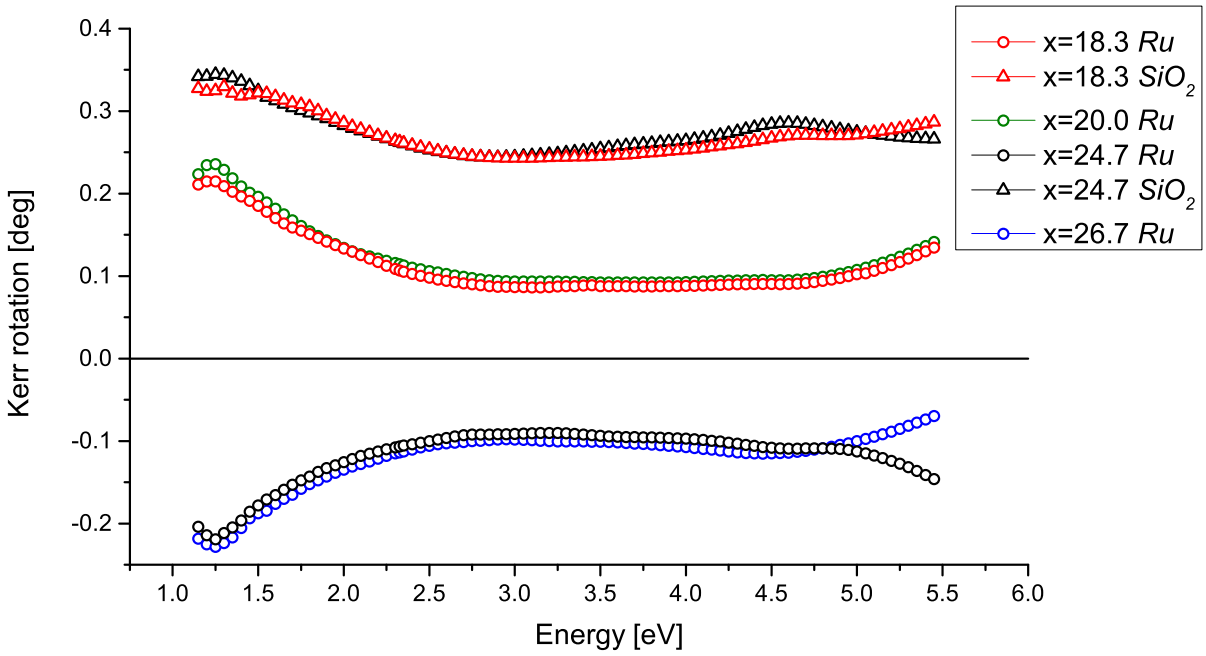

(a) Kerr rotation spectra

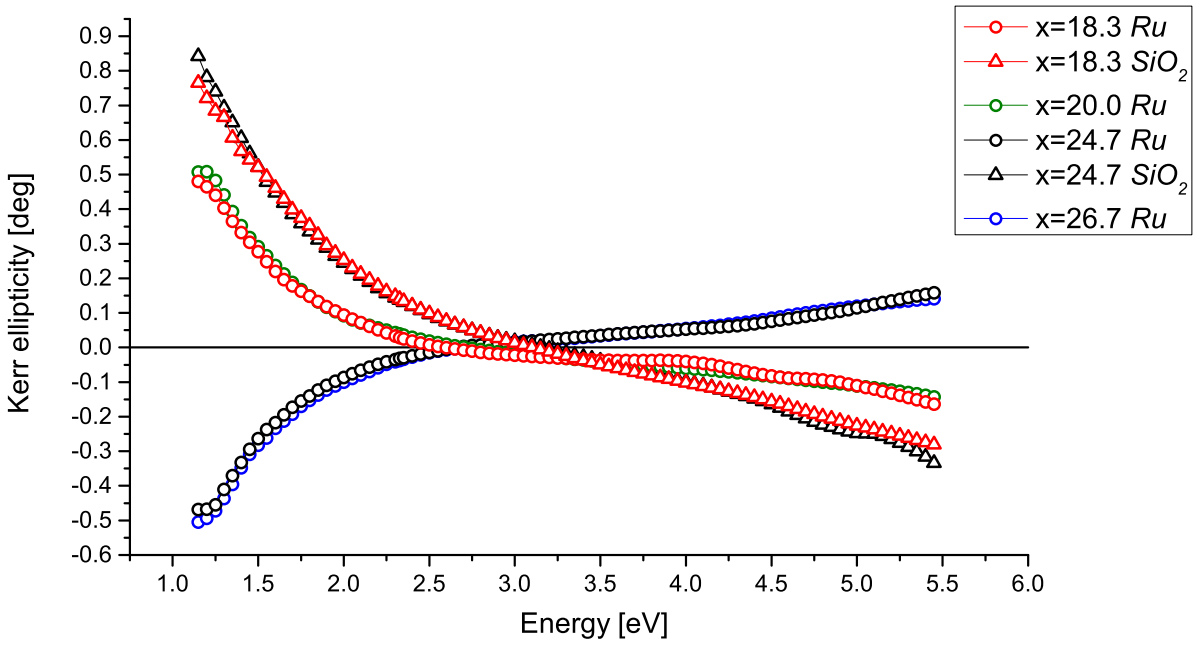

(b) Kerr ellipticity spectra

Figure 4.1: MOKE spectra of measured $GdFe$ samples

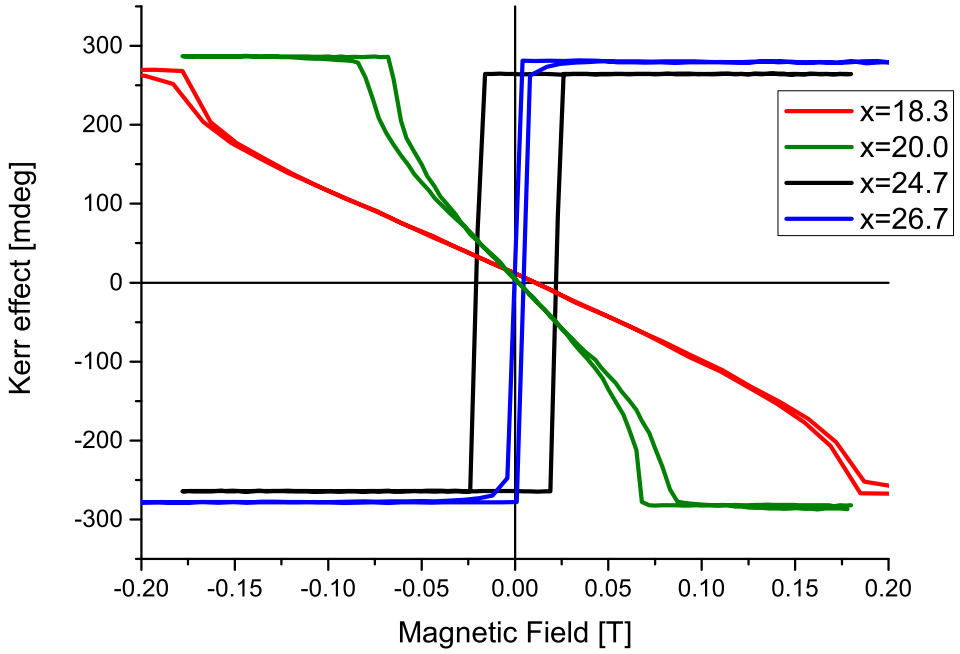

(a) Samples with Ru capping

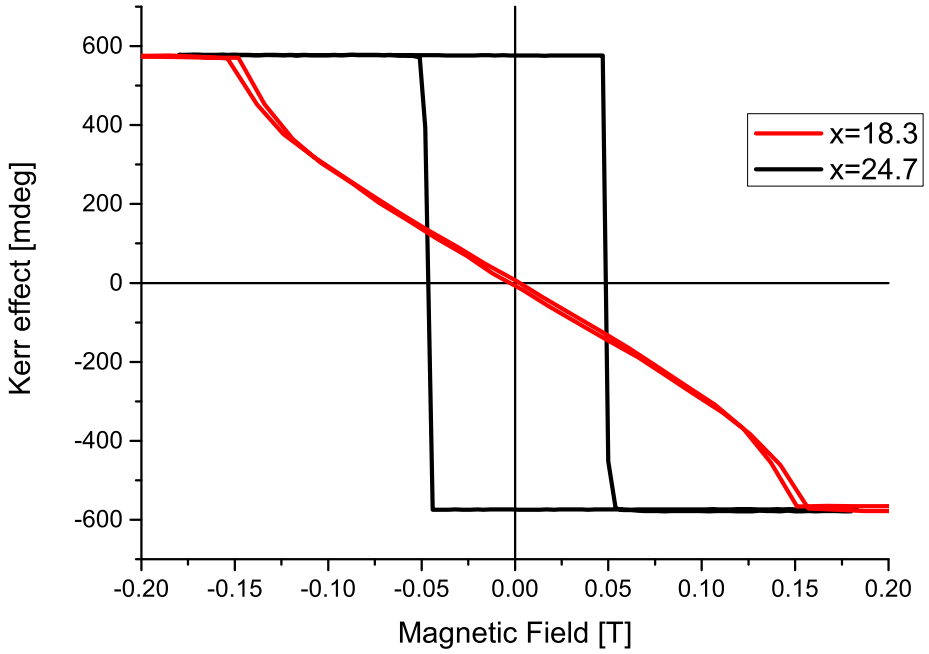

(b) Samples SiO_2 capping

Figure 4.2: Hysteresis curves from MOKE magnetometry at $658\,nm$ ($1.88\,eV$).

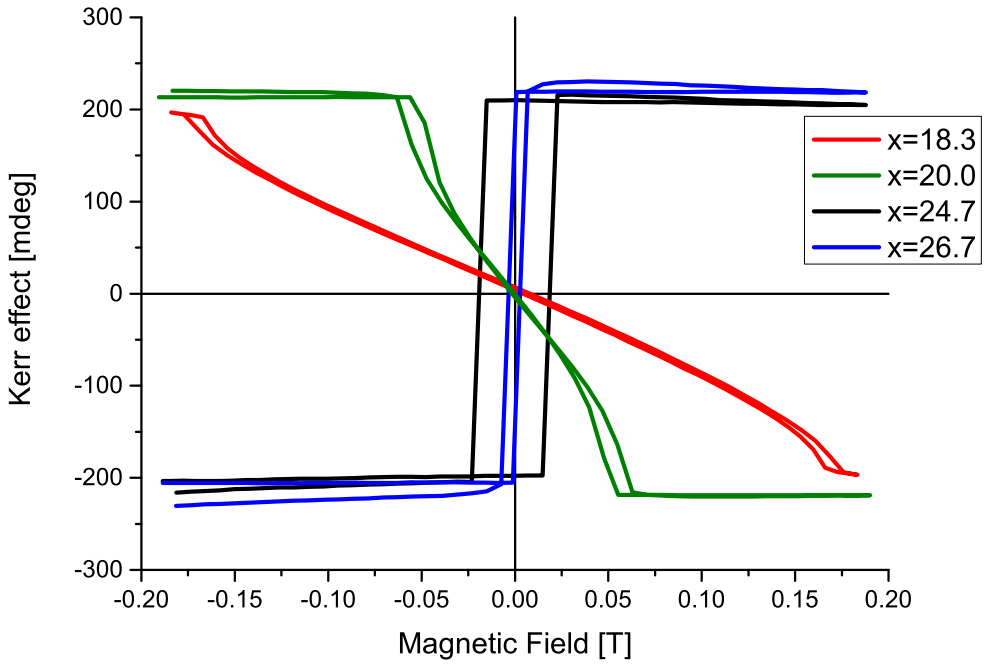

(a) Samples with Ru capping

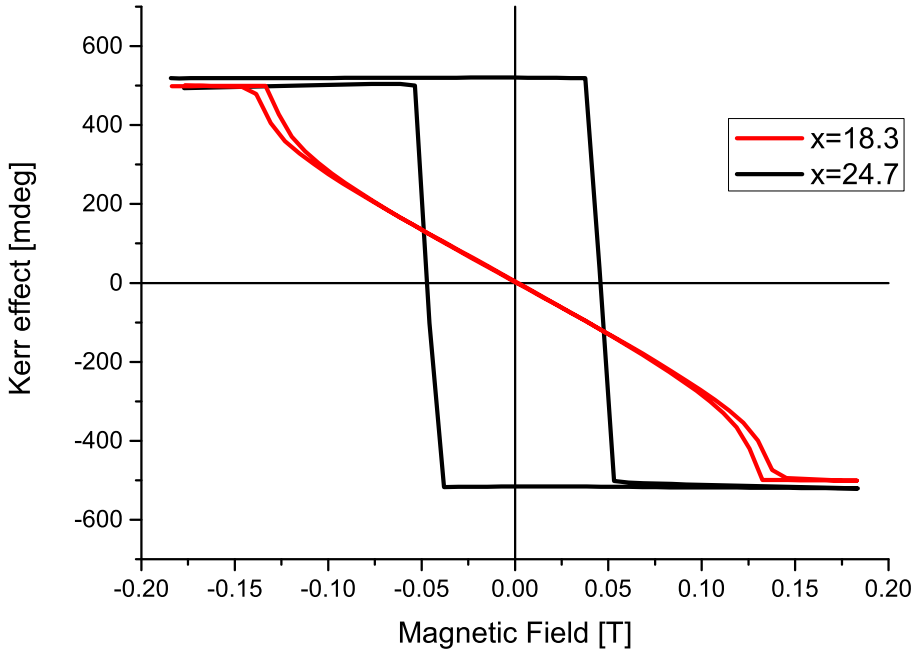

(b) Samples SiO_2 capping

Figure 4.3: Hysteresis curves from MOKE magnetometry at $520\,nm$ ($2.38\,eV$).

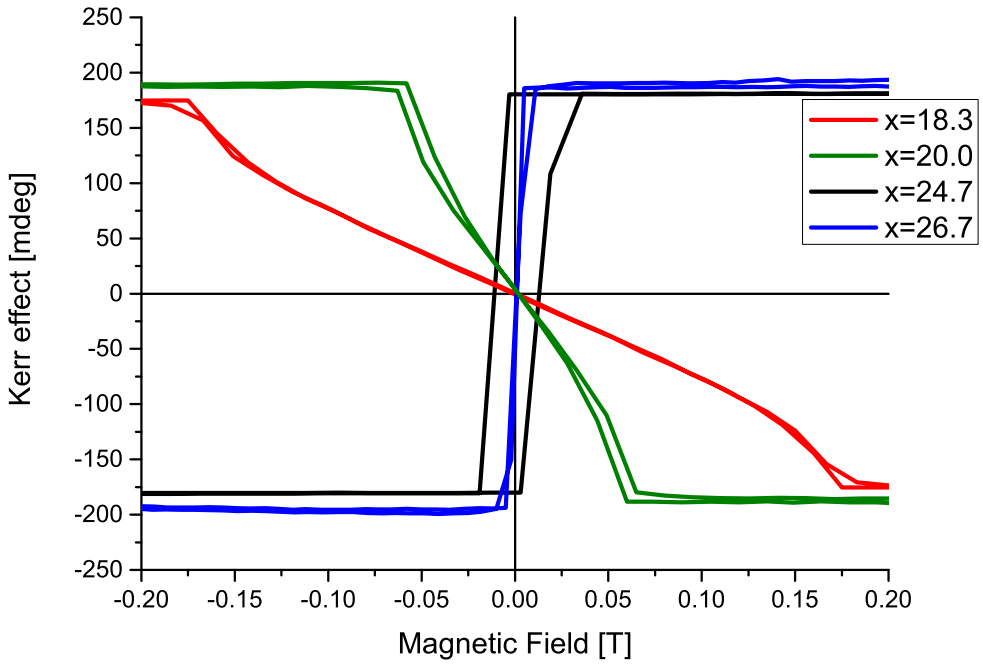

(a) Samples with Ru capping

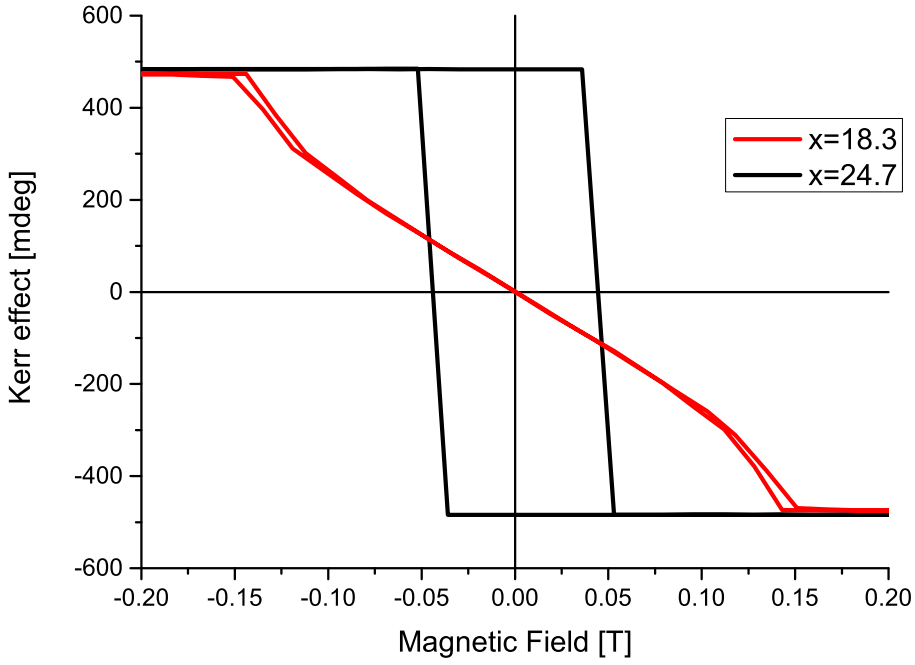

(b) SiO_2 capping samples

Figure 4.4: Hysteresis curves from MOKE magnetometry at $405\,nm$ $(3.06\,eV)$.

4.1.3 Spectroscopic ellipsometry measurements

With SE measurements we determined the spectral dependence of ellipsometric angles from 1 to 6 eV, while measuring under angles of incidence 55°, 60° and 65°. These measurements showed less than 0.6% depolarisation due to to high reflectivity of the samples, and therefore our measurements can be considered very precise.

One of the fitting parameters of SE is the surface roughness, which was determined by AFM. We carried out measurement of samples both with SiO_2 and Ru capping. The result shows that the samples have very smooth surface. This is visualised in Figure 4.5a and 4.5b showing, that the roughness can be neglected, since the profile analysis determined it as less than one nanometer. This also points out that the used sample fabrication method is sufficient for application in MO-SLM pixels which have a high demand on well-defined interlayers. The straight line in Figure 4.5a is a measurement gem.
The results of theoretical modelling of the $GdFe$ and the substrate and capping layers are shown in Figure 4.6a and 4.6a, which plot the spectral dependence of real and imaginary parts of ε_1 of the $GdFe$ layer only. This result is independent on the capping layer. The trend in ε_{1r} of increasing value around 2.9 eV with increased concentration of Gd, means that Gd positively increases the refractive index of the alloy. Whereas the ε_{1i} spectral dependence does not vary much with different components ratio. This behaviour is usually explained by intra-band transitions. The fitting has also proven that nominal thickness of the main layer does not fully agree with the nominal thickness of 100 nm $GdFe$ from the sputtering (the XRR measurement got confirmed). Obtaining the knowledge of the permittivity tensor allows the theoretical prediction of complex physical properties of complicated pixel multilayered nanostructures containing Gd_xFe_{100-x} layer.
The complete results, including computation of off-diagonal element ε_2 of the permittivity tensor using Yeh's formalism from the measurements of Kerr effect and diagonal elements of permittivity tensor and detailed theoretical ellipsometric models provided by E. Jesenská, are about to be published as [40].

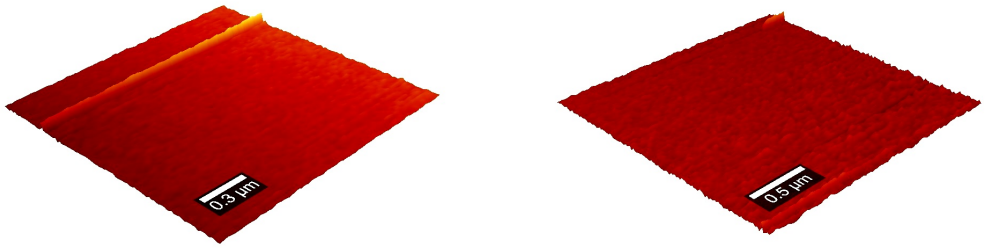

(a) Ru capping sample (b) SiO_2 capping sample

Figure 4.5: AFM measurement of $GdFe$ samples surface.

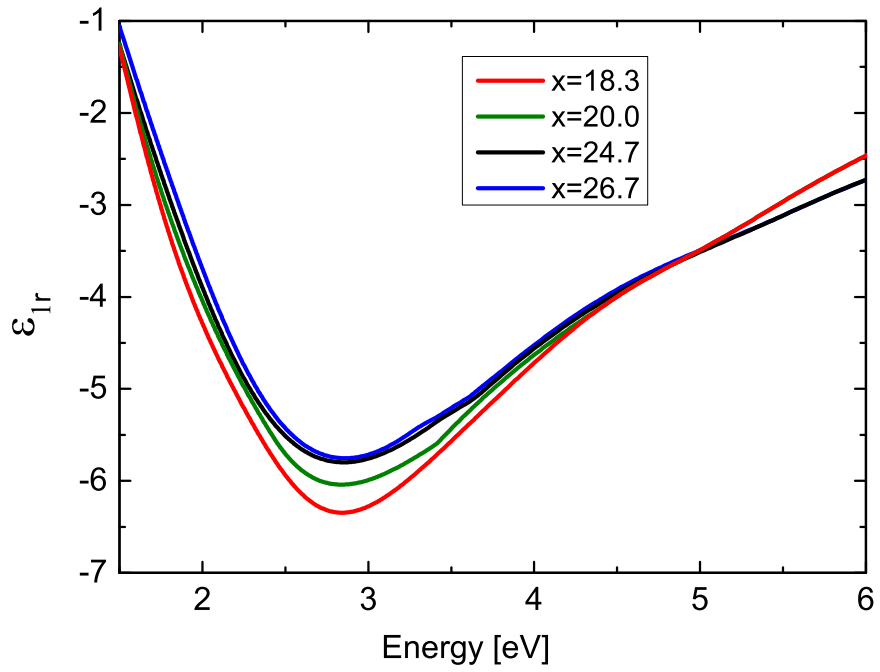

(a) Real part of ε_1

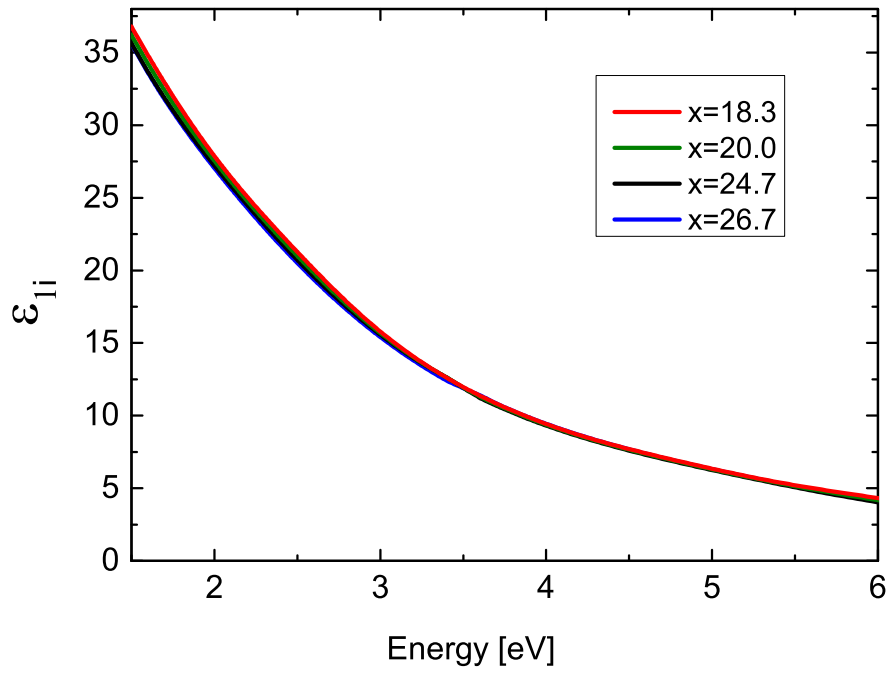

(b) Complex part of ε_1

Figure 4.6: ε_1 spectral dependence of $GdFe$ layer obtained from SE

4.2 Mn_3Ge

The aim of the study of the Mn_3Ge compound was to manage the growth of different phases of Mn_3Ge and observe their MO and optic properties mainly for the tetragonal $D022 - Mn_3Ge$ which has already been studied [28]. Yet its fabrication should be the first step to the future growth of $D019 - Mn_3Ge$, which has not been prepared in the form of thin film yet [37]. In order to be able to deposit determined stochiomtries of a Mn and Ge compound in a magnetron-sputtering machine, a calibration of sputtering rates was needed based on XRR measurements. Consequently, an attempt to grow the $D022 - Mn_3Ge$ was made, with the focus on structural analysis and the MOKE spectra measurement.

4.2.1 Calibration of Mn and Ge targets samples

With calibration samples, we needed to control our deposition sputtering rates from the Mn and the new Ge targets at the sample. The UHV sputtering machine is equipped with a quartz crystal scale which monitors the sputtering rate at a fixed position in the chamber, yet the sample is located in a slightly different place and angle with respect to the targets. Also every target has a different profile of the sputtered atoms beam, so it is necessary to obtain the tooling factor TF of each target. This number is the ratio between the sputtering rate measured at the crystal and at the sample position. By obtaining it via measuring layer thickness on the calibration sample we should be able to have precise sputtering rates of each element at the sample for precise stoichiometry fabrication.

There are many parameters that influence the growth at the sputtering machine. Firstly, current input into the DC diodes and the power input into the RF diodes influence the sputtering rates with a linear dependence. For our calibration we set $125\,mA$ at Mn target on the DC-diode (the crystal measures rate $0.37\,\mathring{A}/s$ with TF set at 62%) and $35\,W$ at Ge target on the RF-diode (the crystal measures rate $0.12\,\mathring{A}/s$ with TF set at 119%). With this basic settings the calibration samples were grown with nominal thickness in Table 4.2 (estimated from the time between sample shutter opening and closing). Two important variables are in the game during sputtering. The Ar gas work pressure P_{Ar} at the chamber can influence the speed with which sputtered species are deposited on the substrate and the temperature T at the sample heater influences the thermodynamics at the substrate surface. We have used different combinations of low/high value of pressure/temperature to find out, how they influence the deposition rates. The stacks of Mn and Ge layers were caped with Ta to prevent oxidation. Si with thermal oxide was selected as a sufficient cheap substrate for the calibration.

Table 4.2: The set of calibration samples with nominal layer thickness T_N

Sample	Substrate	Main layers	Cap. layer	P_{Ar} $[mTorr]$	T $[°C]$
S482	Si/SiO_2	Mn $[17\,nm]$ / Ge $[17\,nm]$	Ta $[2\,nm]$	1.15	RT
S483	Si/SiO_2	Mn $[17\,nm]$ / Ge $[17\,nm]$	Ta $[2\,nm]$	6.3	RT
S484	Si/SiO_2	Mn $[17\,nm]$ / Ge $[17\,nm]$	Ta $[2\,nm]$	1.2	400
S485	Si/SiO_2	Ge $[17\,nm]$	Ta $[2\,nm]$	6.5	400

After the fabrication we have examined the samples by XRR to determine their thickness. That was done by P. Cejpek and Table 4.3 shows the results based on fitting of reflectivity oscillations with theoretical models of given layers. The errors of thickness determinations are derived from errors of fits, so it is important to take in notion the precision of the fits.

Table 4.3: Measured layer thickness T_M from XRR (provided by P. Cejpek).

Sample	Result
Clean Si/SiO_2 substrate	T_C of the SiO_2 layer $=(91.4 \pm 0.1)nm$
S482	Tc of the Ta layer $=(2.7 \pm 0.4)\,nm$ Tc of the Ge layer $=(15.0 \pm 0.2)\,nm$ Tc of the Mn layer $= (18.6 \pm 0.2)\,nm$ Tc of the SiO_2 layer $= (97.1 \pm 0.1)\,nm$
S483	Tc of the Ta layer $=(4.3 \pm 0.1)\,nm$, Tc of the Ge layer $=(12.9 \pm 0.1)\,nm$, Tc of the Mn layer $= (19.4 \pm 0.1)\,nm$ Tc of the SiO_2 layer $=(91.1 \pm 0.1)\,nm$
S484	Sample's interlayers are too rough, oscillations fade away too quickly, it is not possible to determine any valid information
S485	Tc of the Ta layer $= (5.2 \pm 0.4)nm$ Tc of the Ge layer $=(9.3 \pm 0.2)nm$ Tc of the SiO_2 layer $= (83.2 \pm 0.2)nm$

We have, based on this criterion, selected the sample **S483** as the most precise calibration of sputtering rate, therefore we obtain tooling factor of the Ge and Mn targets. Figure 4.7b shows the XRR measurement's results and theoretical layer model fitting. It is apparent that the sample **S483** has its layers defined better than **S482** (and also **S485**), for which better fit was not obtainable. This is caused by the lack of annealing post-deposition process of each layer after their deposition. Good model-experiment match on **S483** points out, that higher pressure helps more precise and better defined deposition of used elements. Higher temperature should only influence different crystallization of the deposited material. Annealing after a new layer position should make the interlayer less rough. The TF were calculated on elements densities as $TF_{Ge} = 75\,\%$ and $TF_{Mn} = 130\,\%$. We have tried out MOKE sectra measurements on **S483**, but the sample did not exhibit any MOKE. We also measured SE of the calibration samples. An attempt to fit the measured ellipsometric angles with theoretical models failed, mainly since the libraries lacked models of such thin layers of the used elements. This would need a deeper research, yet for our further purpose XRR provided a very precise result.

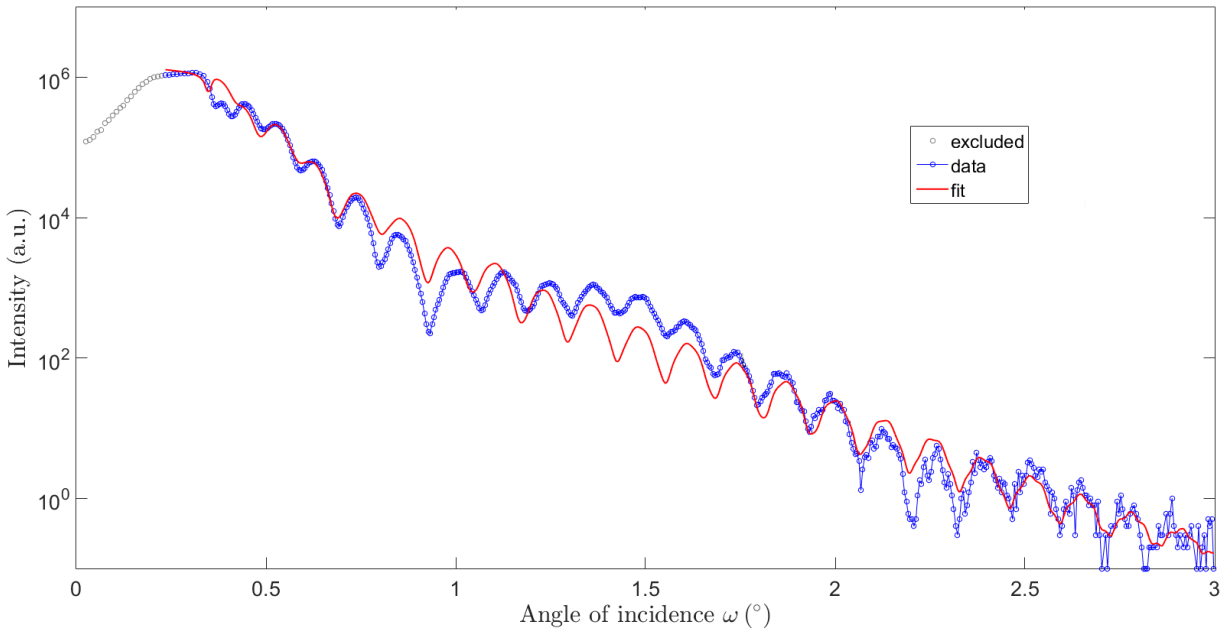

(a) Sample S482

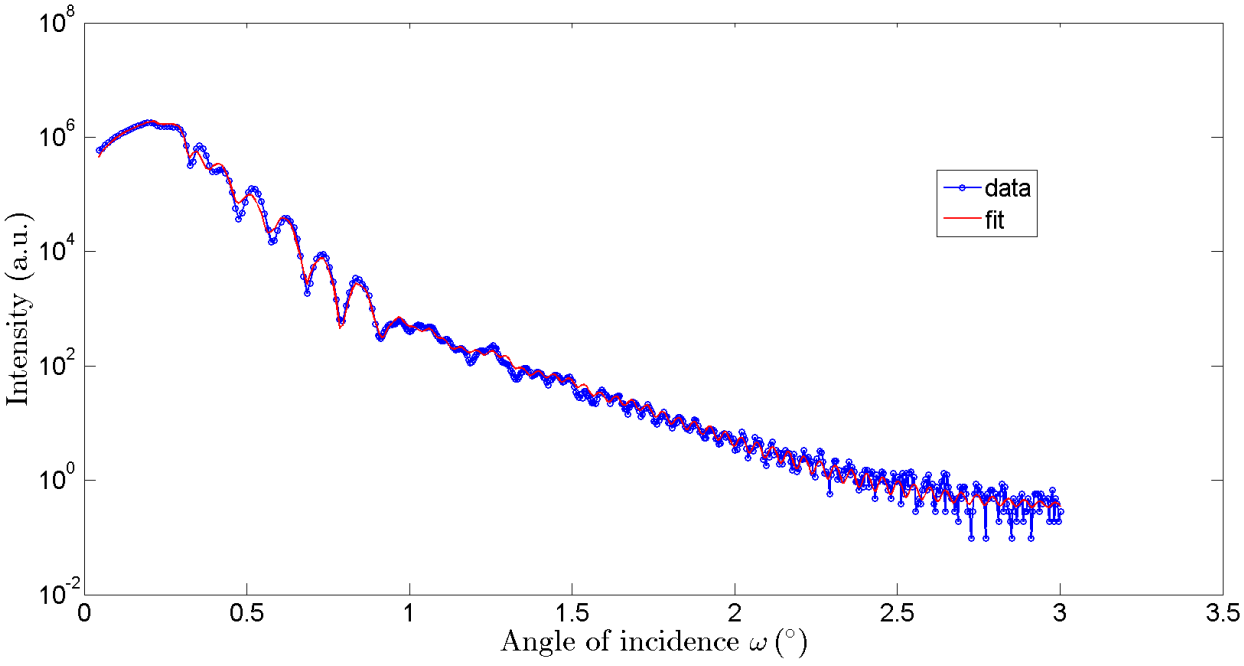

(b) Sample S483

Figure 4.7: XRR reflectivity of the calibration samples (provided by P. Cejpek).

4.2.2 Attempt to grow and study $D022 - Mn_3Ge$

With the precise calibration of the targets in hands, we have made an attempt to fabricate thin layer $D022 - Mn_3Ge$. The widest knowledge was collected about its growth on MgO (001) substrate [30]. There is approximately 10% lattice mismatch between these two materials and we used a Cr buffer layer in order to have a better lattice match at the interlayer. This arrangement is also in accordance with the possible implantation in a MTJ device [27].
The process and samples of this growth attempt are shown in Table 4.4. Based on the calibrated targets' TF values we have set the input current and power on the Mn and Ge targets in the way that the sputtering rates matched the molar ratio $3:1$ of deposited materials. That was with $150\,mA$ at the Mn and $50\,W$ at the Ge target for the stoichiometric ratio with **S501**. We increased/decreased these inputs for the slightly off-stoichiometric **S502** and **S504**. Before the deposition of the main layer at **S503**, both targets had a shortage, so we kept the sample of Cr buffer only for further measurements and comparison. Sputtering rates were re-measured before further deposition after the target cleaning. Annealing steps and temperatures during the growth were followed from [31]. Higher pressure of the Ar gas was used based on the calibration results. Capping layer was done using Cr to prevent the oxidization of the main layer.

Table 4.4: The set of Mn_3Ge samples with nominal figures and fabrication details

Sample	Substrate	Buffer Layer	Main Layer	Cap. layer
S501	MgO (001)	Cr [40 nm]	Mn_3Ge [30 nm]	Cr [5 nm]
S502	MgO (001)	Cr [40 nm]	$Mn_{3+5\%}Ge_{1-5\%}$ [30 nm]	Cr [5 nm]
S503	MgO (001)	Cr [40 nm]	-	-
S504	MgO (001)	Cr [40 nm]	$Mn_{3-5\%}Ge_{1+5\%}$ [30 nm]	Cr [5 nm]
Process Notes	Cleanned with aceton and N_2 gun, annealed at 700°C for 1 hour	Deposition at RT and 1,2 mTorr of Ar, annealed at 700°C for 1 hour	Deposition at 400°C and 5,6 mTorrr of Ar	Deposition at 400°C and 1,4 mTorrr of Ar

The four fabricated samples were measured by the XRD method by V. Holý. These 2θ measurements have observed only MgO and Cr diffraction peaks (in Figure 4.8), no trace of any crystalline form of Mn_3Ge. XRR also points out smaller layer thickness than the nominal. That means that the growth did not succeed. This was also confirmed by the MOKE spectra, which had detected nearly zero signal when compared to measurement error and noise as shown in Figure 4.9. The small deviation from the null line might have its origin in a few atom layer thick crystalline form of Mn.
An attempt to establish a crystalline magnetic phase in the intended Mn_3Ge layer was done by sample **S502** annealing in 450°C in high vacuum of $1 \cdot 10^{-7} Pa$ for two hours. This process did not change the repeated MOKE spectra measurement, it only turned the surface colour from silver to golden, probably by thermal oxidation of the Cr capping. The explanation for the growth failure is not clear.

There is a possible option of a mistake in the calibration (sputtering was done with 4 months gap), the growth pressure might also play a role and the other growth parameters like target current and power need to be tuned. This topic is open for further research.

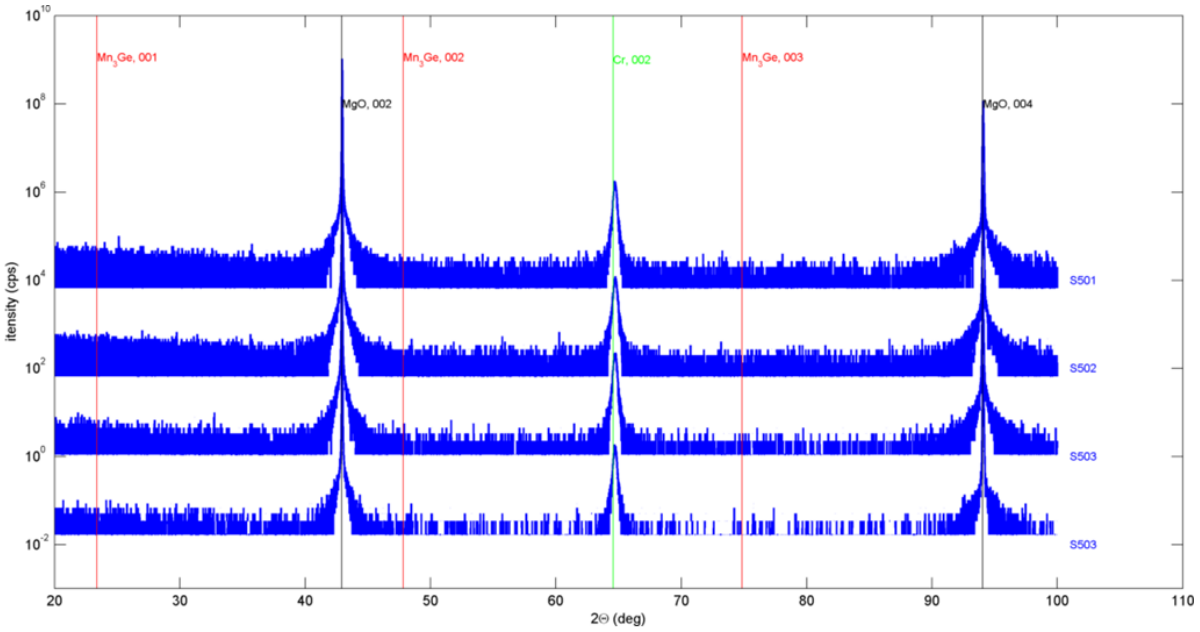

Figure 4.8: XRD of Mn_3Ge samples (provided by V. Holy)

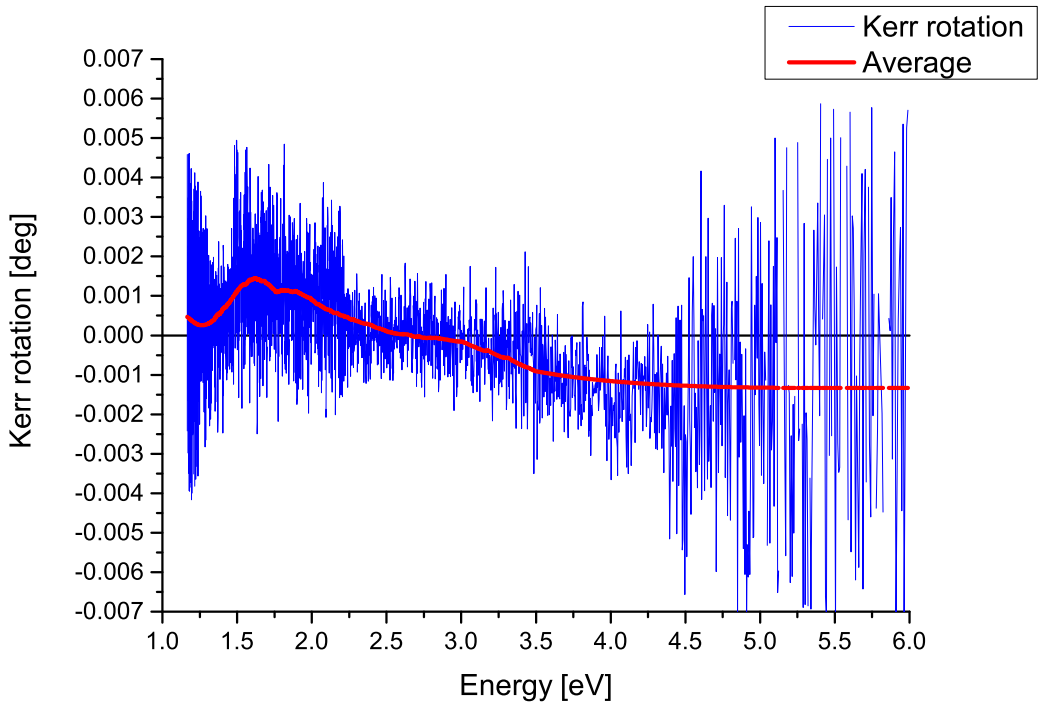

Figure 4.9: Raw plot and Sav.-Gol. average of Kerr rotation measurement of the Mn_3Ge sample **S504**

Conclusion

This work presents a study of characterization and deposition of two novel materials, which can have a significant role in the technological progress. The material $GdFe$ finds its application in the holographic display concept, that uses its Kerr rotation for spatial light modulatiion from spin photonics approach. Whereas Mn_3Ge might be soon found in the magnetoresistive random access memories in the form of magnetic tunnel junction, a structure explained by spintronics.

We have investigated magneto-optic and optical properties of $GdFe$ with magneto-optic spectroscopy and magnetometry. These results gave us an insight into the magnetic response and structure of this alloy. Special emphasis was paid on the concentration of the alloy's components and it was proven that the compensation point and capping layer are important for special magnetization characteristics. Spectroscopic ellipsometry provided us with information about alloy's refractive index (with typical minima around $2.9\,eV$) and absorption (that is decreasing with increasing photon energy). The results of this investigation will have an impact on further development of the prototype of the holographic display where multilayer pixels are fabricated and the information about optical properties of each layer is needed. The results are about to be published [40].

We attempted to grow Mn_3Ge by sputtering and measure it with optical and magneto-optic methods as part of this work. The deposition of precise stoichiometries needed a calibration of targets' sputtering rates for each element. This was carried out using the X-ray reflectivity and the results were implemented into the next growth. We then aimed to fabricate the tetragonal phase of the Mn_3Ge. The attempt has not succeed. That was proven by the X-ray diffraction and Kerr rotation measurements. We have grown an amorphous layer of Mn and Ge mixture with an unknown composition and later annealing of one sample has not made a change in the magnetic properties. The topic of Mn_3Ge needs further research with respect to the method for its growth in various phases and investigation of their physical properties.

To conclude, we have obtained both original results as well as negative ones. This situation shows the snares of the material science, when well prepared samples can bring straight forward results, but the initial growth of a new material can be more similar to alchemy and require a long process of growth conditions tuning.

Bibliography

[1] James Clerk Maxwell. A dynamical theory of the electromagnetic field. *Philosophical Transactions of the Royal Society of London*, 155:459–513, 1865.

[2] J. Peatross and M. Ware. *Physics of Light and Optics*. Brigham Young University, 2015.

[3] M. Nývlt. *Optical interactions in ultrathin magnetic film structures*. PhD thesis, Charles University, Prague, 1996.

[4] Max Born and Emil Wolf. *Principles of Optics: Electromagnetic Theory of Propagation, Interference and Diffraction of Light*. Cambridge University Press, 1999.

[5] John Kerr. XLIII.on rotation of the plane of polarization by reflection from the pole of a magnet. *Philosophical Magazine Series 5*, 3(19):321–343, May 1877.

[6] John Kerr. XXIV.on reflection of polarized light from the equatorial surface of a magnet. *Philosophical Magazine Series 5*, 5(30):161–177, March 1878.

[7] Jeffrey McCord. Progress in magnetic domain observation by advanced magneto-optical microscopy. *Journal of Physics D: Applied Physics*, 48(33):333001, July 2015.

[8] Višňovský Štefan. *Optics in magnetic multilayers and nanostructures*. CRC Taylor & Francis, Boca Raton, 2006.

[9] P. G. van Engen, K. H. J. Buschow, R. Jongebreur, and M. Erman. PtMnSb, a material with very high magneto-optical Kerr effect. *Applied Physics Letters*, 42(2):202–204, January 1983.

[10] Jaroslav Hamrle. Magneto-optical kerr effect (MOKE), October 2014.

[11] Harland Tompkins and Eugene A Irene. *Handbook of Ellipsometry (Materials Science and Process Technology)*. William Andrew, 2006.

[12] GregorioW. Schematic of an atomic force microscope, Wiki Commons 13.10.2016.

[13] Hideaki Adachi. *Handbook of sputter deposition technology : fundamentals and applications for functional thin films, nano-materials and MEMS*. William Andrew, Waltham, MA, 2012.

[14] S. A. Wolf. Spintronics: A spin-based electronics vision for the future. *Science*, 294(5546):1488–1495, November 2001.

[15] Gordon E. Moore. Cramming more components onto integrated circuits. *Electronics*, pages 114–117, 1965.

[16] Tom Simonite. Intel is putting the brakes on Moore's law, August 2016.

[17] M. Mitchell Waldrop. The chips are down for Moore's law. *Nature*, 530(7589):144–147, February 2016.

[18] Andrew D. Kent and Daniel C. Worledge. A new spin on magnetic memories. *Nature Nanotechnology*, 10(3):187–191, March 2015.

[19] T. Jungwirth, X. Marti, P. Wadley, and J. Wunderlich. Antiferromagnetic spintronics. *Nature Nanotechnology*, 11(3):231–241, March 2016.

[20] P. Wadley, B. Howells, J. Zelezny, C. Andrews, V. Hills, R. P. Campion, V. Novak, K. Olejnik, F. Maccherozzi, S. S. Dhesi, S. Y. Martin, T. Wagner, J. Wunderlich, F. Freimuth, Y. Mokrousov, J. Kune, J. S. Chauhan, M. J. Grzybowski, A. W. Rushforth, K. W. Edmonds, B. L. Gallagher, and T. Jungwirth. Electrical switching of an antiferromagnet. *Science*, 351(6273):587–590, January 2016.

[21] Kenichi Aoshima, Hidekazu Kinjo, Kenji Machida, Daisuke Kato, Kiyoshi Kuga, Tomoyuki Mishina, Hiroshi Kikuchi, and Naoki Shimidzu. Three dimensional motion picture technologies. In *2014 IEEE Industry Application Society Annual Meeting*. IEEE, October 2014.

[22] K. i. Aoshima, N. Funabashi, K. Machida, Y. Miyamoto, K. Kuga, T. Ishibashi, N. Shimidzu, and F. Sato. Submicron magneto-optical spatial light modulation device for holographic displays driven by spin-polarized electrons. *Journal of Display Technology*, 6(9):374–380, Sept 2010.

[23] Daisuke Kato, Kenichi Aoshima, Kenji Machida, Akira Emoto, Hidekazu Kinjo, Kiyoshi Kuga, Hiroshi Ono, Takayuki Ishibashi, Hiroshi Kikuchi, and Naoki Shimidzu. Holographic images reconstructed from GMR-based fringe pattern. *EPJ Web of Conferences*, 40:16006, 2013.

[24] Kenichi Aoshima, Hidekazu Kinjo, Kenji Machida, Daisuke Kato, Kiyoshi Kuga, Takayuki Ishibashi, and Hiroshi Kikuchi. Active matrix magneto-optical spatial light modulator driven by spin-transfer-switching. *Journal of Display Technology*, 12(10):1212–1217, October 2016.

[25] Eva Jesenska, Takahiro Hashinaka, Takayuki Ishibashi, Lukas Beran, Jan Dusek, Roman Antos, Kiyoshi Kuga, Ken-ichi Aoshima, Kenji Machida, Hidekazu Kinjo, and Martin Veis. Optical and magneto-optical properties of Gd22Fe78 thin films in the photon energy range from 1.5 to 5.5 eV. *Materials*, 9(1):23, 2016.

[26] I. Radu, K. Vahaplar, C. Stamm, T. Kachel, N. Pontius, H. A. Dürr, T. A. Ostler, J. Barker, R. F. L. Evans, R. W. Chantrell, A. Tsukamoto, A. Itoh, A. Kirilyuk, Th. Rasing, and A. V. Kimel. Transient ferromagnetic-like state mediating ultrafast reversal of antiferromagnetically coupled spins. *Nature*, 472(7342):205–208, March 2011.

[27] Jaewoo Jeong, Yari Ferrante, Sergey V. Faleev, Mahesh G. Samant, Claudia Felser, and Stuart S. P. Parkin. Termination layer compensated tunnelling magnetoresistance in ferrimagnetic heusler compounds with high perpendicular magnetic anisotropy. *Nature Communications*, 7:10276, January 2016.

[28] Huseyin Kurt and J. M. D. Coey. Magnetic and electronic properties of thin films of Mn-Ga and Gn-Ge compounds with cubic, tetragonal and hexagonal crystal structures. In *Heusler Alloys*, pages 157–191. Springer International Publishing, November 2015.

[29] Shigemi Mizukami, Akimasa Sakuma, Atsushi Sugihara, Takahide Kubota, Yukio Kondo, Hiroki Tsuchiura, and Terunobu Miyazaki. Tetragonal D022Mn3Ge epitaxial films grown on MgO(100) with a large perpendicular magnetic anisotropy. *Applied Physics Express*, 6(12):123002, December 2013.

[30] A. Sugihara, S. Mizukami, Y. Yamada, K. Koike, and T. Miyazaki. High perpendicular magnetic anisotropy in D022Mn3Ge tetragonal heusler alloy films. *Applied Physics Letters*, 104(13):132404, March 2014.

[31] A Sugihara, K Suzuki, S Mizukami, and T Miyazaki. Structure and magnetic properties of tetragonal Heusler D022Mn3Ge compound epitaxial films with high perpendicular magnetic anisotropy. *Journal of Physics D: Applied Physics*, 48(16):164009, April 2015.

[32] A. Sugihara, K. Z. Suzuki, T. Miyazaki, and S. Mizukami. Magnetic properties of ultrathin tetragonal Heusler D022Mn3Ge perpendicular-magnetized films. *Journal of Applied Physics*, 117(17):17B511, May 2015.

[33] Atsushi Sugihara, Kazuya Suzuki, Terunobu Miyazaki, and Shigemi Mizukami. Effect of process temperature on structure and magnetic properties of perpendicularly magnetized D022Mn3Ge thin films on a Cr buffer layer. *Japanese Journal of Applied Physics*, 54(8):083001, July 2015.

[34] Atsushi Sugihara, Kazuya Suzuki, Terunobu Miyazaki, and Shigemi Mizukami. Epitaxial growth of hard ferrimagnetic Mn3Ge film on rhodium buffer layer. *Metals*, 5(2):910–919, June 2015.

[35] H. Kurt, N. Baadji, K. Rode, M. Venkatesan, P. Stamenov, S. Sanvito, and J. M. D. Coey. Magnetic and electronic properties of D022Mn3Ge (001) films. *Applied Physics Letters*, 101(13):132410, September 2012.

[36] Jakub Zelezny, Yang Zhang, Claudia Felser, and Binghai Yan. Spin-polarized current in non-collinear antiferromagnets Mn3X (X = Ga, Ge, Sn, Rh, Ir, Pt). arXiv:1702.00295 2017.

[37] A. K. Nayak, J. E. Fischer, Y. Sun, B. Yan, J. Karel, A. C. Komarek, C. Shekhar, N. Kumar, W. Schnelle, J. Kubler, C. Felser, and S. S. P. Parkin. Large anomalous hall effect driven by a nonvanishing berry curvature in the noncolinear antiferromagnet Mn3Ge. *Science Advances*, 2(4):e1501870–e1501870, April 2016.

[38] Dang Duc Dung, Wuwei Feng, Yooleemi Shin, and Sunglae Cho. Magnetism and transport properties of α-Mn structure Mn3Ge thin film. *Journal of Applied Physics*, 109(7):07C310, April 2011.

[39] M Deb, E Popova, A Fouchet, and N Keller. Magneto-optical Faraday spectroscopy of completely bismuth-substituted Bi3Fe5O12garnet thin films. *Journal of Physics D: Applied Physics*, 45(45):455001, October 2012.

[40] Eva Jesenska, Takayuki Ishibashi, Lukas Beran, Martin Pavelka, Kiyoshi Kuga, Ken ichi Aoshima, Kenji Machida, Hiroshi Kikuchi, Naoki Shimidzu, and Martin Veis. Optical and magneto-optical properties of $GdxFe$(100-x) thin films close to the compensation point. 2017. Unpublished Manuscript.

List of Abbreviations

AFM = Atomic force microscopy

DC = Direct current

FE = Faraday effect

GMR = Giant magnetoresistance

MTJ = Magnetic tunnel junction

MO = Magneto-optic

MOKE = Magneto-optic Kerr effect

MO-SLM = Magneto-optic spatial light modulator

MRAM = Magnetoresistive random access memories

PCSA = Polarizer-compensator-sample-analyzer

RF = Radio frequency

SE = Spectroscopic ellipsometry

STS = Spin transfer switching

STT = Spin transfer torgue

XRD = X-ray diffraction

XRR = X-ray reectivity